PHYSICAL REVIEW FLUIDS **5**, 103501 (2020)

Thermal convection in octagonal-shaped enclosures

Prabir Kumar Kar,[1] Yada Nandu Kumar,[2] P. K. Das,[3] and Rajaram Lakkaraju[4,*]
[1]*School of Energy Science & Engineering, Indian Institute of Technology Kharagpur, Bengal-721302, India*
[2]*Centre for Theoretical Studies, Indian Institute of Technology Kharagpur, Bengal-721302, India*
[3]*Department of Mechanical Engineering, Indian Institute of Technology Kharagpur, Bengal-721302, India*
[4]*Computational Mechanics Group, Department of Mechanical Engineering,*
Indian Institute of Technology Kharagpur, Bengal-721302, India

(Received 27 October 2019; accepted 3 September 2020; published 7 October 2020)

Flow-reversal phenomena in a classical two-dimensional (2D) Rayleigh-Bénard convection, in a square enclosure, are usually explained through growth and merging of diagonally opposite counterrotating corner rolls. To probe further the corner-roll growth dynamics, we have altered the square enclosure edges by additional slanted conduction walls, so that the enclosure resembles an octagonal shape. We have performed a series of 2D numerical simulations by varying the slanted wall inclination angle (α) from 0° to 45°, to construct a detailed flow map in thermal convection in a range $5 \times 10^5 \leqslant \mathrm{Ra} \leqslant 10^8$ and $0.8 \leqslant \mathrm{Pr} \leqslant 2.0$, where Ra is the Rayleigh number and Pr is the Prandtl number. Depending on Ra, Pr, and α, flow features in the octagonal enclosure can exist in the form of a uniform circulation, a two-roll, a mixed, a periodic, a quasiperiodic, or multiple flow states superimposed on each other. The flow reversals in the octagonal enclosure take place in several ways, for example, by the ejection of mushroom-shaped plumes alternatively from the opposite slanted walls at low Ra ($\approx 10^5$) and high Pr (≈ 2), by the corner-roll growth at high Ra ($\approx 10^8$) and low Pr (≈ 1.2), and by the dipole at high Ra ($\approx 10^8$) and high Pr (≈ 2). Strikingly, the dimensionless flow-reversal frequency scales linearly with an increase in α, and the slope varies from 1.04 at low $\mathrm{Ra} = 5 \times 10^5$ to 0.328 at high $\mathrm{Ra} = 10^8$. We have shown the flow reversals are a consequence of competition between the dipole (a two-roll state where a cold roll sits above a hot roll) and the quadrupole (the four corner rolls) modes with the monopole mode. A uniform circulation with flow-reversal results if the quadrupole mode wins, and a two-roll state with a reversal results, if the dipole wins. At high Ra ($\geqslant 10^8$), the dipole strengthens, and the core bulk region shows hydrodynamic instabilities in the form of turbulent-like engulfments. We have uncovered the mechanism responsible for the observed engulfments due to the increase in turbulence production in the core bulk region by the buoyancy. As a result, we have observed that total heat transport also increases up to 14% when α is varied from 0° to 45°.

DOI: 10.1103/PhysRevFluids.5.103501

I. INTRODUCTION

Fluid motion driven by temperature gradient is of fundamental interest due to its wide range of applications in solar energy [1,2], nuclear reactors [3], heat-recovery systems [4], room ventilation [5], and nature-inspired phenomena [6–9]. A classical example of thermal convection is a fluid layer heated from below and cooled from above, widely known as Rayleigh-Bénard (RB) convection [10–13], in which if the applied temperature difference (ΔT) across the fluid layer

---

[*] Corresponding author: rajaram.lv@gmail.com

©2020 American Physical Society

is higher than a certain critical value [14], one may see convective motions in the form of rolls, thermal plumes, and large-scale circulations (LSCs) [15–17]. The control parameters which govern the flow in RB convection are, namely, the Rayleigh number (Ra), defined as the ratio of buoyancy and damping mechanisms (i.e., viscous and thermal diffusion); the Prandtl number (Pr), defined as the ratio of the kinematic viscosity to the thermal diffusivity; and the aspect ratio (Γ), defined as the ratio of width to height of the enclosure. At low Ra ($10^5 \leqslant \mathrm{Ra} < 10^6$), the convective motions show distinct flow patterns and spatiotemporal chaos [18,19], whereas thermal plumes and organized motions [20] are observed at slightly high Ra ($> 10^6$). With a further increase in Ra, large-scale motions and random fluctuations develop in the flow with unexpected flow transitions [11]. For very high Ra, if one hypothesizes the convection similar to the Kolmogorov theory of turbulence, then universality in the small-scale motions would be expected [21], and the scientific community has engaged to verify it [22]. In recent studies on high Ra convection in small aspect ratio ($\Gamma < 1$) enclosures [23,24] and in other high Reynolds number flows such as in rotating cylinders [25,26] and spherical enclosures [27], the coexistence of different flow states was observed. The wall boundaries of the enclosure played a significant role in the generation of the multiple flow states [23,24], especially, flow reversals like the sloshing, azimuthal meandering, corner-roll growth, and other forms [15,28,29]. Understanding flow reversals has major implications for nature-inspired buoyancy-driven flows such as the Earth's geomagnetic fields, atmospheric circulation, and oceanic currents [30–33].

First, we briefly overview earlier theoretical works which have highlighted the flow-reversals phenomena in thermal convection [34,35]. For example, Sreenivasan *et al.* [34] have proposed flow reversals as a Brownian process with the switching of two metastable states, whereas Araujo *et al.* [35] have derived simplified a Lorenz-like model by balancing force and thermal energy on a single plume. The flow-reversal frequency in Ref. [35] was shown proportional to $\mathrm{Ra}^{0.44\pm0.01}\,\mathrm{Pr}^{-(0.65\pm0.01)}$ in the range $10^9 \leqslant \mathrm{Ra} \leqslant 10^{12}$ and $0.7 \leqslant \mathrm{Pr} \leqslant 316$. However, 3D experiments [29,36] revealed the flow reversals were due to the azimuthal meandering and the sloshing modes, whereas the growth of the corner rolls is responsible for the reversal in two dimensions [16,17]. The flow reversals were observed only in a limited range of Ra and Pr parameter space, and they were not possible at low Pr ($\leqslant 0.6$) due to high thermal diffusion and at high Ra ($> 10^9$) due to strengthened LSC [15]. To explain the mechanism of flow reversals, Chandra and Verma [16,17] have used the Fourier decomposition technique to represent the LSC in the form of various modes and their interactions. The LSC takes different forms such as the monopole (ellipse), the dipole (as two vertically or horizontally stacked rolls), or the quadrupole (as four corner rolls). In general, the flow reversals in a square enclosure consist of three phases, namely, the accumulation, the release, and the acceleration [37]. In the accumulation phase, the corner rolls draw thermal energy from the boundary layers and grow with time. In the release phase, the potential energy transforms into the LSC's kinetic energy. In the acceleration phase, the LSC self-organizes itself into the form of a large roll assisted by two additional corner rolls, and thus completes the flow-reversal cycle. During the flow reversals, both the velocity and the temperature fields show coherent oscillations with a mean period (which depends on Ra and Pr) different from the plume free-fall time by at least two orders of magnitude. The overall convective heat flux shows a sudden jump from a positive to a negative and vice versa [16,17]. However, recent experiments [38] on a thin vertical disk surprisingly showed flow reversals even when the corner rolls were absent. Similarly, Chen *et al.* [39,40] have shown that flow reversal in a square enclosure is possible by placing inclined (or slanted) partitions, which have eliminated the corner rolls. The flow-reversal frequency (f) in Ref. [40] showed a power-law relation in the form of $f t_E \propto \mathrm{Ra}^{\phi}$, where ϕ is the scaling exponent, and t_E is the large eddy turnover time. Interestingly, around the transition Rayleigh number Ra_T ($\approx 2 \times 10^8$), ϕ changes from -1.08 to -2.83 when the slanted walls were absent, and from -1.53 to -5.05 when the walls were present. The lower limits of ϕ are for $\mathrm{Ra} < \mathrm{Ra}_T$ and the higher limits for $\mathrm{Ra} > \mathrm{Ra}_T$. The change in the scaling exponent is attributed to the bulk zone instabilities, instead of the corner-roll growth. The precise mechanism for the emergence of these instabilities is yet unexplored to our best knowledge, and our work is a step in exploring those features.

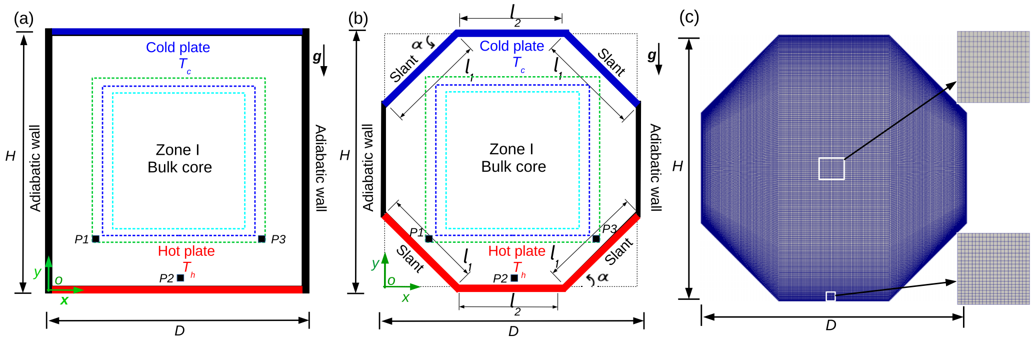

FIG. 1. Schematics of a square (a) and an octagonal enclosure (b). The square is D in width and H in height, with $D = H$. We have inscribed an octagon in a square as a geometry and studied thermal convection. The slanted (or inclined) walls are of length l_1, which make an angle α with the horizontal walls (of length l_2). Note, hot walls (in red) at bottom, cold walls (blue) at top, and adiabatic sidewalls (black). The walls of the octagonal enclosure satisfy $2l_1 \cos\alpha + l_2 = D$. The geometry origin is taken at the bottom left corner, and directions are x in the horizontal direction and y in the vertical direction. The gravity acts along the negative y direction. Three square subdomains (shown by dash lines) are chosen to extract the Fourier modes. The subdomain areas in dimensionless square units are 0.4624 (for green box), 0.36 (for blue box), and 0.2704 (for cyan box). The blue box region with $0.2D \leqslant x \leqslant 0.8D$ and $0.2H \leqslant y \leqslant 0.8H$ is considered as a bulk region. Small black square symbols represent numerical probe locations, and their (x, y) coordinates are the probe $P1$ at $(0.1465, 0.0852)$, the probe $P2$ at $(0.5, 0.02)$, and the probe $P3$ at $(0.8535, 0.0852)$. (c) A typical computational mesh used for a regular octagonal enclosure (with $\alpha = 45^\circ$). Total number of computational meshes used is 102 400. Close-up views of computational mesh near the bottom wall and in the core bulk region are also shown. Slant represents additional conduction walls used.

From the above discussion, a natural question arises whether a flow reversal is due to the corner-roll growth in the 2D enclosure, or is it due to the bulk core region instability? How does that transformation happen? To answer that, we need to understand the interaction of the corner rolls with the enclosure walls. The corner rolls in a square enclosure grow in size with time by exchanging heat with the thermal boundary layers near the conduction walls, whereas the insulated vertical walls apply strong viscous resistance not to let corner rolls move away from their initial location. In that situation, if we relax the wall conditions, mainly, either by providing additional heat to the corner rolls or by changing the wall corner angle, will that lead to any significant change in the corner-roll growth process? We can guess that supplying additional heat to the corner rolls may help in its growth and, thus, frequent flow reversals. Also, the corner rolls may be washed away by the LSC if the wall corner angle is changed from 90° to any other value. To understand whether the corner rolls ultimately govern the flow reversals or not, we have explored a geometry in the form of an octagonal enclosure (see Fig. 1) different from the square. We have studied thermal convection in the proposed geometry in the range $5 \times 10^5 \leqslant \mathrm{Ra} \leqslant 10^8$ and $0.8 \leqslant \mathrm{Pr} \leqslant 2$. The octagonal enclosure is very similar to the square in terms of the thermal and velocity boundary conditions; however, additional heat can enter or leave from the slanted (or inclined) walls. Total conduction wall length in the octagonal enclosure is longer than the adiabatic wall length. We have systematically varied the slanted wall angle (α) from 0° to 45°. The lower limit represents a square enclosure and the upper limit a regular octagon. On one hand, the proposed octagonal geometry is an addition to the existing studies on thermal convection. On the other hand, it allows us to explore the role played by the corner rolls. Even at a fundamental level, our geometry helps to mark which aspects of thermal convection may be universal and which may depend on the spatial confinement. From our simulations, we have found both flow reversals and heat transport increase (up to 14%), if we use the octagonal enclosure instead of a square cell. For thermal convection in the octagonal enclosures, we have explored answers to the following questions: Why does the reversal frequency increase? Are the corner rolls still responsible for the flow reversals? What are the dominant flow features? What explains an increase in heat transport? What is the role played by the slanted walls in changing the overall flow features? How do thermal plumes from the horizontal and slanted walls interact with the bulk core region?

We have organized our work as follows: In Sec. II we have introduced the octagonal geometry, the mathematical framework, and the computational methods. In Secs. III and IV we have compared flow features and dominant flow modes for the square and the octagonal enclosures, respectively. We have addressed the flow-reversal frequency in Sec. V and heat transport in Sec. VI. By using the vorticity dynamics and the turbulent kinetic energy budget, we have explained the core bulk region instabilities in Sec. VII. Finally, in Sec. VIII we have summarized our results.

II. GOVERNING EQUATIONS AND COMPUTATIONAL METHOD

We have shown schematics of a square and an octagonal enclosure in Figs. 1(a) and 1(b), respectively. The bottom conduction walls (marked in red) are maintained at a temperature T_h (hot), and the top walls (marked in blue) at T_c (cold). The sidewalls (marked in black) are thermally insulated. We have maintained a no-slip velocity condition on all the walls. The square enclosure has a width D, equals to height H, such that the aspect ratio $\Gamma = \frac{D}{H} = 1$. In the octagonal enclosure, we have additional conduction walls of length l_1, arranged at an inclination angle (α) to the horizontal conduction walls of length l_2. We have chosen l_1 and l_2 in such a way that an octagon is always inscribed in a square. The geometric relation $2l_1 \cos\alpha + l_2 = D$ is always enforced with a fixed length $l_2 = 0.4142D$. Note, $l_1 < l_2$ for $\alpha < 45^\circ$, and $l_1 = l_2$ for $\alpha = 45^\circ$.

The conservation of mass, momentum, and the thermal energy equations under the Boussinesq approximation are

$$\nabla \cdot \mathbf{u} = 0, \tag{1}$$

$$\frac{\partial \mathbf{u}}{\partial t} + \mathbf{u} \cdot \nabla \mathbf{u} = -\frac{1}{\rho_m}\nabla p + \nu \nabla^2 \mathbf{u} + \mathbf{g}\beta(T - T_m), \tag{2}$$

$$\frac{\partial T}{\partial t} + \mathbf{u} \cdot \nabla T = \kappa \nabla^2 T, \tag{3}$$

where $\mathbf{u} = (u, v)$ is the velocity field, T is the temperature, and p is the dynamic pressure after subtracting the hydrostatic component. We have taken the fluid properties at the reference (mean) temperature T_m, at which the density is ρ_m, the kinematic viscosity is ν, the thermal expansion coefficient is β, and the thermal diffusivity is κ. The acceleration due to gravity $\mathbf{g}$ acts in a negative y direction. The operators $\frac{\partial}{\partial t}$, ∇, and ∇^2 are the time derivative, the spatial derivative, and the Laplacian, respectively. The Rayleigh number, $\mathrm{Ra} = |\mathbf{g}|\beta \Delta T H^3/\nu\kappa$, is defined based on maximum separation distance between the conduction walls (H) and the temperature difference $\Delta T = T_h - T_c$. The Prandtl number is $\mathrm{Pr} = \nu/\kappa$. The governing equations (1) to (3) are solved by using an open-source finite-volume code OpenFOAM [41]. We have used the first-order implicit Euler scheme to integrate temporal terms and the Gauss linear scheme for the spatial terms. In our simulations, nonuniform meshes are used with a minimum of 16 to 20 grid points to resolve the boundary layers.

In Fig. 1(c) we have shown a typical computational mesh used in our simulations for $\mathrm{Ra} = 10^8$ and $\mathrm{Pr} = 0.8$. We have shown the grid resolutions used to resolve core bulk and the boundary layer zones in insets of the same figure. The maximum Courant number in our simulations never exceeded a value of 0.2. We have varied control parameters in the range $5 \times 10^5 \leqslant \mathrm{Ra} \leqslant 10^8$, $0.8 \leqslant \mathrm{Pr} \leqslant 2$, and $0^\circ \leqslant \alpha \leqslant 45^\circ$. The total number of computational cells in our simulations vary from 26 244 (for $\mathrm{Ra} = 10^5$) to 102 400 (for $\mathrm{Ra} = 10^8$). The free-fall velocity, $U = \sqrt{|\mathbf{g}|\beta \Delta T H}$, the characteristic time, $\tau = H/U$, and the characteristic angular momentum per unit mass, $L_{\mathrm{char}} = UH$, are used to nondimensionalize variables mentioned at a later stage. After reproducing the RB convection results in a square enclosure (both the global Nusselt number and the flow features), we have proceeded further to explore details on convection in the octagonal enclosures. We have also carried out a

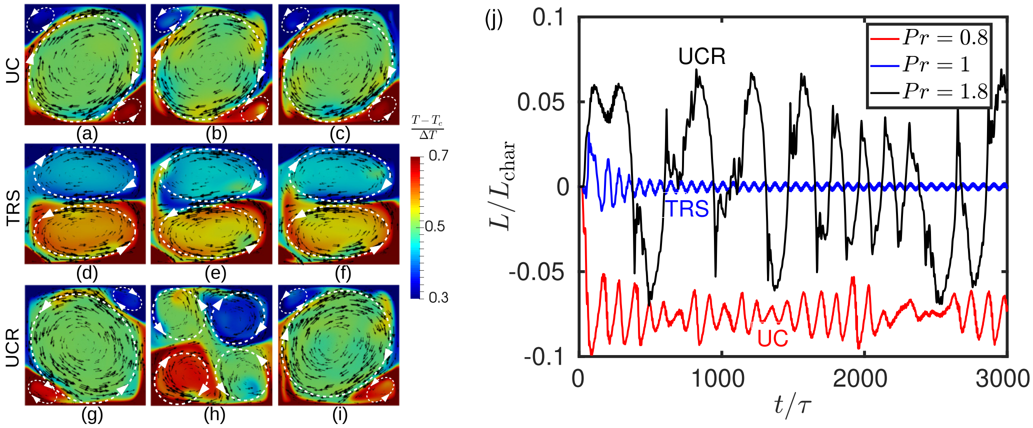

FIG. 2. Left panels for instantaneous temperature and velocity fields. Panels (a) to (c) for uniform circulation (UC) at Pr = 0.8, panels (d) to (f) for a stable two-roll structure (TRS) at Pr = 1, and panels (g) to (i) for uniform circulation with reversals (UCR) at Pr = 1.8. Time increases from left to right in each row; see animation 1 in the Supplemental Material [45]. Color bar for dimensionless temperature, $(T - T_c)/\Delta T$, which ranges from 0.3 (blue) to 0.7 (red). Black small arrows for the velocity field. White dashed lines with arrows indicate large-scale (dominant) rolls with their direction of rotation and approximate size. In right panel (j), normalized angular momentum vs time: UC state at Pr = 0.8 (red), TRS at Pr = 1 (blue), and UCR at Pr = 1.8 (black). Simulations for a square enclosure at Ra = 10^7.

grid-independence test for Ra = 10^8, Pr = 0.8, and $\alpha = 45^\circ$ using two different mesh sizes 65 536 and 102 400, for which the calculated Nusselt numbers are within 0.8% error. The numerical code used in our work is validated extensively in other earlier works [42–44]. We have used the overline of a quantity to represent a statistically stationary state or a long-term average for more than $10\,000\tau$.

III. FLOW FEATURES IN A SQUARE ENCLOSURE

In this section, we describe flow features observed in a square enclosure ($\alpha = 0^\circ$). In Figs. 2(a) to 2(i) we have shown instantaneous temperature fields and velocity vectors at a fixed Ra = 10^7. The shown flow features represent three different dynamical states, namely, the uniform circulation (UC) at Pr = 0.8, the two-roll structure (TRS) at Pr = 1, and the uniform circulation with reversals (UCR) at Pr = 1.8. In the UC state, we have observed a single large-scale roll in the form of an ellipse with its major axis aligned on one of the diagonals, and two small counterrotating corner rolls confined on the other diagonal. The observed UC state is stable without any flow reversals in the time range from 1000τ to $20\,000\tau$, and the core bulk region is at a uniform temperature ($\approx T_m$) see Fig. 2(a) to Fig. 2(c). The corner rolls rotate opposite to the direction of LSC, and continuously exchange heat with the conduction walls. The thermal plumes frequently detach from the conduction walls, swept along the LSC, or get trapped by the corner rolls. Sometimes, the plumes may intermittently burst into the core bulk region. For Pr $\ll$ 1, the thermal boundary layers are thick in comparison to the viscous boundary layers [15], and due to that the corner rolls, even if present, may not exchange heat by the convective motions. For Pr $\gg$ 1, the thermal boundary layers are thin in comparison to the viscous boundary layers, and thus, the corner rolls do not grow [15]. In our simulations, we found the stable UC state, without corner-roll growth in the range $0.7 \leqslant \mathrm{Pr} \leqslant 0.95$ and $5 \times 10^5 \leqslant \mathrm{Ra} \leqslant 10^8$. Note, the stable or unstable state behavior can be revealed only by evolution of the disturbances, and within our simulation time limits, i.e., for more than $20\,000\tau$, we did not observe any flow reversal in the mentioned UC state.

For $1 \leqslant \mathrm{Pr} \leqslant 1.6$, we have observed a two-roll state (TRS), where a cold roll (of high density) floats stably over a hot roll (of low density). The falling cold and the rising hot plumes collide at the midpoint of the insulated wall to form a stagnant-like region. The interface between the hot and the cold rolls in the core bulk zone shows flapping like oscillations; see Fig. 2(d) to Fig. 2(f). Notably, the two rolls are asymmetric in the left-right directions about the enclosure vertical midline, and they support additional four tiny rolls at the corners. By further increasing $\mathrm{Pr}(\geqslant 1.8)$, the corner rolls grow unevenly and develop into the uniform circulation state with flow reversals (UCR); see Fig. 2(g) to Fig. 2(i). With an increase in time, the corner rolls grow in size and squeeze the LSC by breaking it into two parts. At that stage, the corner rolls (or the quadrupole) span the enclosure completely, and the LSC halts. We have shown the mentioned flow states in animation 1 in the Supplemental Material [45].

To understand the flow reversals in a better way, we have calculated global angular momentum per unit mass concerning the enclosure center as $L(t) = \langle (x - 0.5H)v(x, y, t) - (y - 0.5H)u(x, y, t)\rangle$, where $\langle\cdot\rangle$ represents the area average. Any sudden jump from a positive to a negative value (or vice versa) on the angular momentum signal indicates the flow reversal. From Ref. [46], we can note that for each flow reversal, the flow should persist in the other direction (of rotation) for at least one eddy turn over time. In Fig. 2(j) we have shown dimensionless L versus time for the discussed UC, TRS, and UCR states. In the UC state, L shows the same sign (here it is negative) but with fluctuations. In the case of TRS, the angular momentum is negligible with, $L \approx 10^{-3} L_{\mathrm{char}}$. In the UCR state, L fluctuates highly with time from a positive to a negative value with sudden jumps, which indicates the cessation-led chaotic reversals [15,47]. The average time duration spent by the large-scale motion in either of the directions represents mean flow-reversal time, and we found the flow reversals take place approximately after every 415τ for $\mathrm{Ra} = 10^7$ and $\mathrm{Pr} = 1.8$. In Ref. [16], the mean flow-reversal time for $\mathrm{Ra} = 2 \times 10^7$ and $\mathrm{Pr} = 1$ is mentioned as 0.6 times the thermal diffusive time units, which corresponds to $0.6\tau\sqrt{\mathrm{Ra}\,\mathrm{Pr}} \approx 2683\tau$. The observed difference in mean flow-reversal time between our simulations and Ref. [16] is due to an abrupt change in flow features for a given small variation in Ra and Pr values. In the latter part of this section, we show that $\mathrm{Ra} = 2 \times 10^7$ and $\mathrm{Pr} = 1$ corresponds to the combined UCR and occasional TRS state, whereas at $\mathrm{Ra} = 10^7$ and $\mathrm{Pr} = 1.8$, it is the UCR with the mixed-mode state. Based on Ra and Pr values, the mean flow-reversal time varies.

To highlight timescales involved with the flow reversals, here we briefly revisit some of the important works [48–50]. Howard [48] has proposed an analytical model in which the thermal boundary layer thickness (δ) near the conduction walls becomes unstable with time, and the thermal plumes detach at a frequency, $f_H \sim \kappa/\delta^2$. Just for discussion, if the local boundary layer thickness grows to half of the enclosure size, i.e., $\delta \approx H/2$, then $f_H \sim 4\kappa/H^2$, which corresponds to a mean flow-reversal time $\frac{1}{f_H} = \tau(\frac{\delta}{H})^2\sqrt{\mathrm{RaPr}} \approx 1060\tau$ at $\mathrm{Ra} = 10^7$ and $\mathrm{Pr} = 1.8$. One can also estimate the boundary layer thickness based on the time-averaged wall thermal gradient computed at the enclosure vertical midline. For $\mathrm{Ra} = 10^7$ and $\mathrm{Pr} = 1.8$, we found the boundary layer thickness, $\delta_{\mathrm{DNS}} \approx H/24$, based on the time-averaged temperature at the midline. Then the corresponding frequency, $f_{\mathrm{DNS}} \sim \kappa/\delta^2_{\mathrm{DNS}}$, and the time period $\frac{1}{f_{\mathrm{DNS}}} \approx 3.81\tau$. Note, the observed mean flow-reversal time in the UCR state ($\equiv 415\tau$) is different from the Howard's estimation by an order of magnitude, indicating the thermal boundary layer instabilities alone cannot explain the flow reversals. Villermaux [49] has also proposed a 2D deterministic model, in which the incoming thermal plumes cause the boundary layer instabilities, which are carried along the enclosure periphery by the LSC. The unstable thermal plumes in the upper and the lower boundary layers interact through a delayed nonlinear coupling, and the plumes emit alternatively at a frequency $f_V = 1/(2\tau)$ or a time duration $\frac{1}{f_V} = 2\tau$. Recently, Brown and Ahlers [50] have shown that the LSC deviates from its preferred orientation when the resonant frequency is minimum around the local potential, i.e., $f_A \equiv U/H$, which corresponds to a period $1/f_A \approx \tau$. From the above discussion, we can note that the mean reversal time observed in a 2D square enclosure in the UCR state is very different from the coherent oscillations observed through either the thermal boundary layer instabilities or the associated coupling mechanisms. Note, the flow reversals observed in the UCR state take place chaotically, and any estimation of the mean flow-reversal time is an approximation considered in the time-averaged sense.

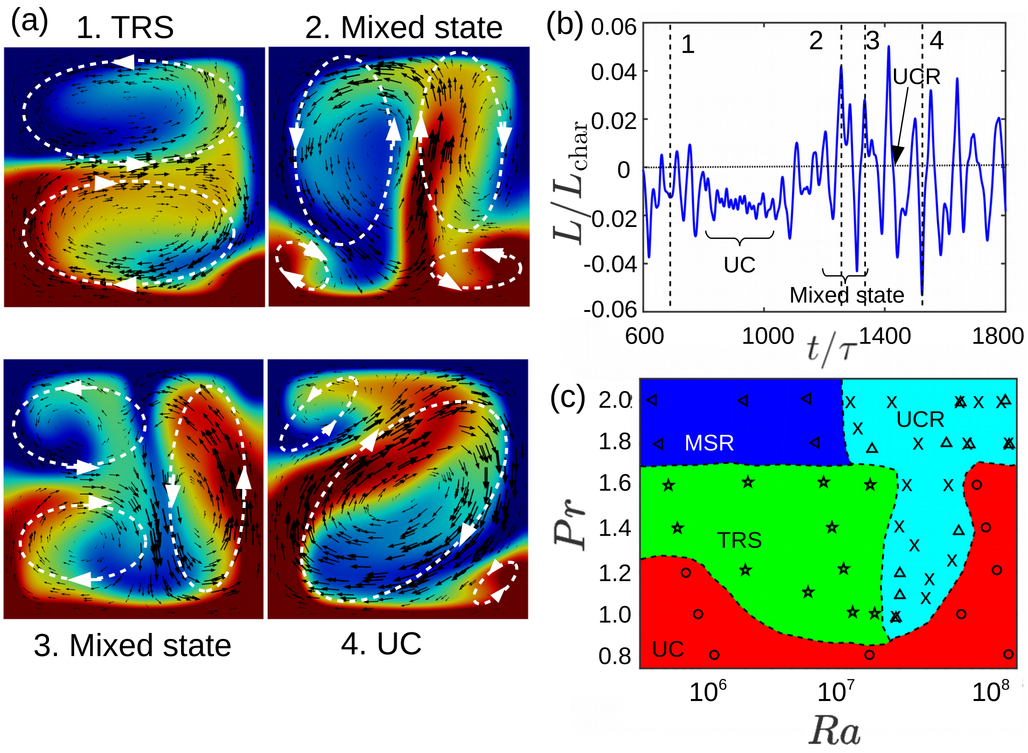

FIG. 3. (a) Instantaneous thermal and velocity fields in a square enclosure at $\mathrm{Ra} = 5 \times 10^5$ and $\mathrm{Pr} = 2$: (1) for two-roll state (TRS), (2 and 3) for a mixed state (MS), and (4) for a uniform circulation state (UC). White dashed lines with arrows indicate large- and small-scale rolls with their direction of rotation and approximate size. (b) Angular momentum vs time. Vertical dash lines in angular momentum plot indicate the time at which panel (a) snapshots are taken. (c) Flow map pattern on Ra-Pr plane. Symbols are circles for UC, pentagrams for TRS, upward triangles for UCR, and leftward triangles for MSR. Black crosses correspond to flow reversals mentioned in Sugiyama *et al.* [15]. To guide the eye, we have shown the hand-drawn demarcation regions with dashed lines.

By decreasing Ra from 10^7 to 10^6 and $1.8 \leqslant \mathrm{Pr} \leqslant 2$, we have observed a mixed roll state with flow reversals (MSR); see Fig. 3(a). In this MSR state, the monopole, the dipole, and the quadrupole interact with each other. We have observed the thermal plumes can rise or fall along the enclosure midline in addition to the sidewalls. We have provided more details of the flow fields in animation 2 in the Supplemental Material [45]. In Fig. 3(b) we have shown the angular momentum versus time in the MSR state (which is a combination of higher modes). To have a better idea of possible flow states in a square enclosure, we have demonstrated a flow map on the Ra-Pr plane in Fig. 3(c). There we have drawn boundaries for the possible four states in the chosen range of parameters. The UC and the TRS are stable states and do not show any flow reversals, whereas the MSR and the UCR states show sudden (or abrupt) flow reversals. The UCR state is present only in a narrow parameter range, i.e., $10^7 \leqslant \mathrm{Ra} \leqslant 10^8$ and $1 \leqslant \mathrm{Pr} \leqslant 2$, consistent with the findings of Sugiyama *et al.* [15]. The mixed state with reversal is visible in the range $5 \times 10^5 \leqslant \mathrm{Ra} < 10^7$ and $\mathrm{Pr} \geqslant 1.7$.

IV. FLOW FEATURES IN AN OCTAGONAL ENCLOSURE

By using an octagonal enclosure instead of a square cell, we have observed flow states and the reversals even at low $\mathrm{Ra}(< 10^6)$. In Fig. 4(a) instantaneous temperature and velocity fields for

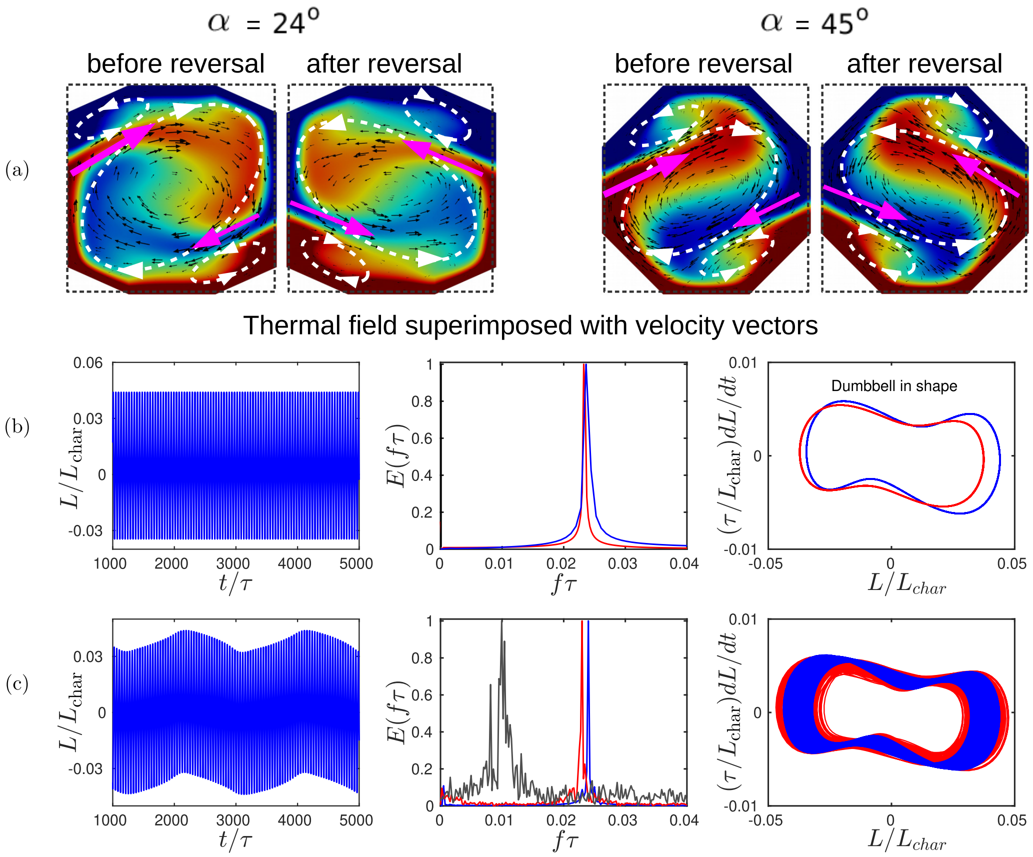

FIG. 4. (a) Instantaneous temperature and velocity fields in octagonal enclosures at $\mathrm{Ra} = 5 \times 10^5$ and $\mathrm{Pr} = 2$. A quasiperiodic reversal state (QPR) for $\alpha = 24^\circ$, and a periodic reversal state (PR) for $\alpha = 45^\circ$. In the same panel, snapshots before and after the flow reversal are also shown. Magenta arrows indicate mushroom-shaped plume ejections. In panels (b) and (c), angular momentum vs time, spectral energy (E) vs frequency (f), and phase plot of L vs dL/dt are shown. Note, variables are shown as dimensionless. (b) Periodic reversal (PR) with $\alpha = 45^\circ$, with a blue line for $\mathrm{Ra} = 5 \times 10^5$, red line for $\mathrm{Ra} = 6 \times 10^5$ and $\mathrm{Pr} = 2$. (c) The same but a blue line for $\mathrm{Ra} = 5.55 \times 10^5$ and $\mathrm{Pr} = 1.8$, red line for $\mathrm{Ra} = 10^6$ and $\mathrm{Pr} = 2$, and gray line for $\mathrm{Ra} = 7.143 \times 10^6$ and $\mathrm{Pr} = 1.4$ for QPR with $\alpha = 45^\circ$.

$\alpha = 24^\circ$ (left panels) and 45° (right panels) are shown. Instead of a mixed state reversal (as observed in a square), we have observed quasiperiodic flow reversals (QPR) for $\alpha = 24^\circ$, and periodic flow reversals (PR) for $\alpha = 45^\circ$. In both cases, two mushroom-shaped thermal plumes eject alternatively from the side inclined walls and drive the LSC. We find long corner rolls on the slanted walls, which are different from that observed in the square enclosure. The giant mushroom-shaped plumes enter the core bulk region and release a significant amount of thermal energy; see animation 2 in the Supplemental Material [45]. It is interesting to understand whether the plume detachment drives the flow reversals or whether it is driven by hydrodynamic instabilities in the bulk core region.

In Figs. 4(b) and 4(c) we have shown global angular momentum (L) with time. The Fourier transform-based energy spectra (E) computed for L shows a peak at a frequency $0.024/\tau$ in the case of the periodic reversal (PR), and two peaks at $0.024/\tau$ and $0.0005/\tau$ in the case of the quasiperiodic reversal (QPR). Note, the flow-reversal frequency is high in the octagonal enclosure by an order of magnitude compared to the same in a square cell. To give the dynamical system's perspective, we have also shown as dimensionless L versus $\frac{dL}{dt}$ in the same figure. By increasing Ra from 5×10^5 to

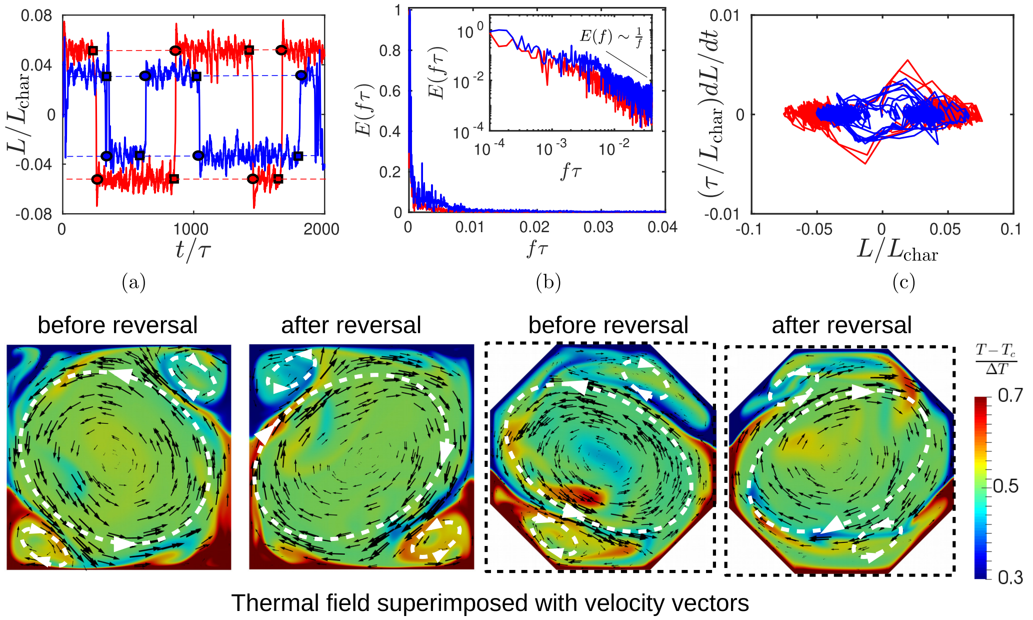

FIG. 5. Comparison of flow reversals in a square ($\alpha = 0^\circ$) and octagonal ($\alpha = 45^\circ$) enclosures at $\text{Ra} = 10^8$ and $\text{Pr} = 1.8$. In top panels: (a) angular momentum vs time, (b) spectral energy (E) vs frequency (f), and (c) phase plot of L vs dL/dt are shown. Red lines for the square enclosure and blue lines for octagon ($\alpha = 45^\circ$). Note, variables are shown in as dimensionless. Time spent in a given state (in which L is nearly constant) is measured between a circle followed by a square symbol. Inset of panel (b) indicates $E \sim 1/f$ at high frequencies. Bottom panels for snapshots of thermal and velocity fields (for before and after flow reversals).

10^6, the closed orbits on L versus dL/dt show nonunique curves with dumbbell-like shapes, which indicate that the flow reversals may be governed by a low-dimensional, weakly nonlinear damped oscillator [49,51].

In Fig. 5 we have compared instantaneous thermal fields before and after a flow reversal for $\alpha = 0^\circ$ and 45°, at a relatively high Ra ($= 10^8$). In the octagonal enclosure, the corner rolls move freely without anchored to the walls; see animation 3(a) and 3(b) in the Supplemental Material [45]. The quadrupole competes with the monopole in the square enclosure, whereas the dipole does that in the octagonal enclosure. Due to the dipole action, thermal plumes of a length comparable to the enclosure size engulf into the core bulk region. From the same figure, we can note that the energy spectrum shows a power-law relation in the form of $E(f) \propto f^{-\eta}$, where η is the spectral slope. A zero spectral slope corresponds to the white noise with no correlation in time, whereas $\eta = 2$, corresponds to the random walk process with no correlation between increments [52]. A spectral slope of $\eta = 1$ is a unique process that shows long-range dependence, and it is not a result of any linear stochastic differential equation by either integration or differentiation. Moreover, the spectral slopes in the range $0.5 < \eta < 2$ represent multifractal processes [52], which are governed by the nonlinear stochastic equations. We also observed zig-zag orbits on L versus $\frac{dL}{dt}$, which indicate the existence of a chaotic attractor in the flow.

In Fig. 6 we have shown a flow map for the octagonal enclosures (with different slanted angles $\alpha = 12^\circ$, 24°, and 45°) on the Ra-Pr plane. In addition to the possible four flow states such as the UC, the TRS, the MSR, and the UCR, we have observed additional flow states in the form of periodic reversals (PR), quasiperiodic reversals (QPR) and two-roll state reversals (TRSR). As α increases from 0° to 45°, an additional two-roll state and a quasiperiodic state emerge in the range

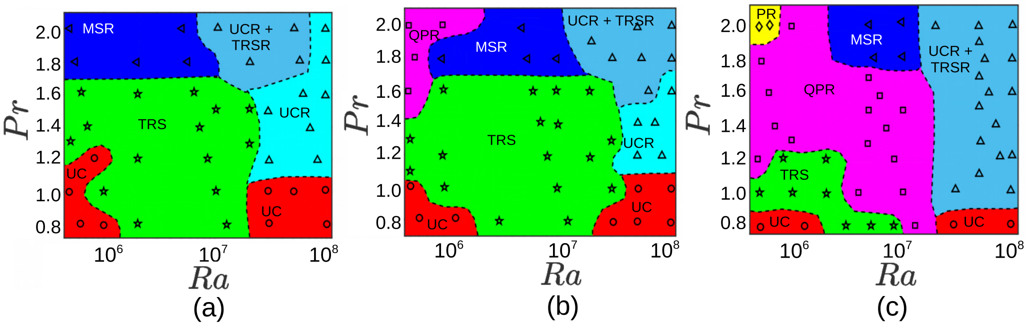

FIG. 6. Flow pattern map on Ra-Pr plane for octagonl enclosures: (a) $\alpha = 12^\circ$, (b) $\alpha = 24^\circ$, and (c) $\alpha = 45^\circ$. Seven distinct flow states such as uniform circulation (UC), uniform circulation with reversal (UCR), stable two-roll state (TRS), mixed state reversal (MSR), periodic reversal (PR), quasiperiodic reversal (QPR), and a combination of UCR+TRSR states are observed. Symbols are for UC (in circles and shaded red), UCR (upward triangles shaded in cyan), TRS (in pentagrams shaded green), MSR (in leftward triangles shaded blue), QPR (in squares shaded magenta), UCR+TRSR (in upward triangles shaded dark cyan) states, and PR (in diamonds shaded yellow). To guide the eye, hand-drawn curves are shown to demarcate the flow states.

$2 \times 10^6 < \mathrm{Ra} < 2 \times 10^7$ and $0.8 \leqslant \mathrm{Pr} \leqslant 1.6$. For large slanted wall angles ($\alpha \geqslant 36^\circ$), most of the flow map is shared by the quasiperiodic state at low Ra ($\leqslant 10^7$) and by the UCR+TRSR states at high Ra ($> 3 \times 10^7$). At high Pr (> 1.8) and very low Ra ($< 10^6$), a state in the form of periodic flow reversals appears for $\alpha = 45^o$. The mixed state, which is visible at high Pr (> 1.8), is narrowed on the flow map with an increase in α.

The Fourier mode decomposition is one of the popular choices to extract the energy content and the large-scale flow features [16,17,53]. A particular Fourier mode can be computed from the vertical velocity as

$$\hat{v}_{(m,n)}(t) = \iint v(x, y, t)\cos(m\pi x)\sin(n\pi y)\,dx\,dy, \tag{4}$$

where $\hat{v}_{(m,n)}(t)$ is the instantaneous mode amplitude with the mode having m rolls in the x direction and n rolls in the y direction. The incompressibility condition connects both the vertical and horizontal velocity components; therefore, one of them is sufficient to understand the flow behavior [16,17,44,47,54]. The Fourier mode (1,1) corresponds to the monopole, and the (2,2) corresponds to the quadrupole. The (1,2) and the (2,1) modes correspond to a two-roll structure in the form of a dipole. Any other modes such as (1,3) and (3,1) consist of three roll structures. Also, the mentioned Fourier decomposition does not satisfy the no-slip condition [16], and it is strictly applicable for a rectangular or a square domain with the periodic boundary conditions. First, we have identified three square subdomains separately in the core bulk region of the enclosure (see Fig. 1) to extract the Fourier modes. The (x, y) limits of the green square zone ranges from $x = 0.16D$ to $0.84D$ and $y = 0.16H$ to $0.84H$. Similarly, the (x, y) limits of the cyan square zone ranges from $x = 0.24D$ to $0.76D$ and $y = 0.24H$ to $0.76H$. If we mention limits in terms of the area spanned by a square, then the green dash line covers a larger area (of 0.4624 square units), and the cyan covers a smaller area (of 0.2704 square units). The blue dash line covers an area of 0.36 square units, which is between the green and cyan lines (or limits). We have carefully chosen these subdomains so that the large-scale modes are not absent due to the presence of random (or turbulent-dominated) fluctuations. We have estimated the instantaneous Fourier modes in each of the domains with the integration limits taken on the respective domain of interest. We found the mode amplitude shows a similar trend for all three subdomains; see Fig. 25 in the Appendix. With these inferences, we have described the Fourier mode results in our work here based on the blue square subdomain (which is between the green and cyan domains).

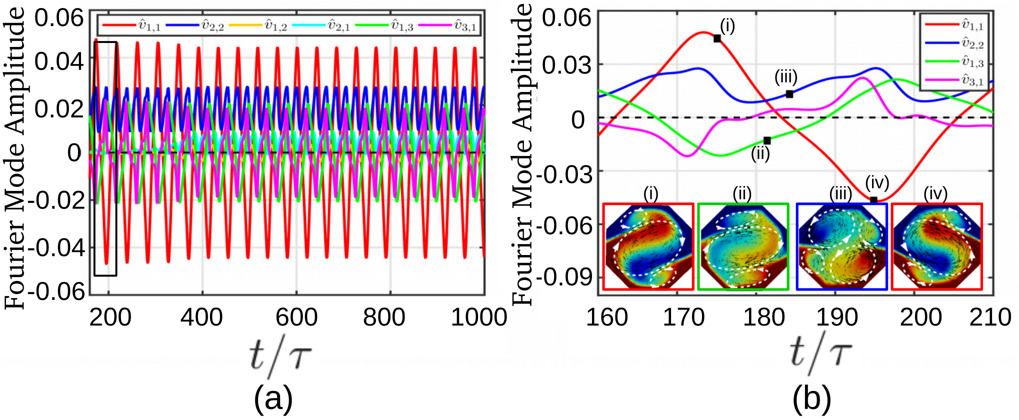

FIG. 7. Fourier mode amplitude vs time in the PR state for $\alpha = 45°$, $\mathrm{Ra} = 5 \times 10^5$, and $\mathrm{Pr} = 2$. Zoomed view of highlighted rectangular box in panel (a) is shown in panel (b). Instantaneous temperature and velocity fields at different times (i), (ii), (iii), and (iv) are shown in insets.

In Fig. 7 we have shown instantaneous Fourier mode amplitudes of the modes (1,1), (2,2), (1,2), (2,1), (1,3), and (3,1), during a periodic flow reversal in the octagonal enclosure. The monopole (1,1) is dominant most of the time except during a flow reversal. The quadrupole (2,2) always shows a positive amplitude. The mode (2,2) shows in-phase oscillation during the LSC formation and the out-phase oscillation while breaking it. However, the modes (1,3) and (3,1) show out-of-phase oscillations with the mode (1,1). We have seen similar mode dynamics, even in the case of the QPR state. In the case of the MSR state, the dominant mode switches between (1,1) and (1,2) chaotically; see Fig. 26 in the Appendix.

At high $\mathrm{Ra}(\geqslant 3 \times 10^7)$ and for $\mathrm{Pr} \geqslant 1$, we have observed chaotic flow reversals in both the square and the octagonal enclosures; see Fig. 8. The UCR state in the octagonal enclosure is shorter in time duration and smaller in the Fourier mode amplitude when compared to the same in the square enclosure. In Figs. 8(c) and 8(d) we have shown zoomed views of the UCR and the TRSR states. With an increase in α, the importance of the modes (1,2) and (2,1) increases, and the mode (2,2) decreases. We have shown instantaneous thermal fields during the UCR, and the TRSR states in the insets of Figs. 8(c) and 8(d), respectively.

Flow reversals in the square enclosure are identified mainly from the monopole mode (1,1) when the mode amplitude changes sign from the positive to the negative or vice versa [16]. Due to the positive and negative fluctuations in the mode amplitudes, we have computed the root-mean-square (RMS) amplitude for each of the modes. In Fig. 9(a) we have shown RMS of a particular mode (m, n) in comparison to the mode (1,1), as a function of α. In the square enclosure, the quadrupole mode (2,2) is 60% in strength when compared to the monopole (1,1), whereas the modes (3,1) and (1,3) have strengths 38% and 20%, respectively. The dipoles (1,2) and (2,1) are weak and have a strength less than 10%. With an increase in α, the quadrupole strength decreases from 60% to 45%, whereas the modes (3,1) and (1,3) strength increases to 40%. The dipoles (1,2) and (2,1) strengthen with an increase in α, and their strengths can even reach up to 80%. The importance of the dipole mode becomes evident beyond $\alpha > 12°$.

During a flow reversal, the kinetic energy (which is proportional to the mode amplitude square) redistributes from the monopole to the other flow modes and vice versa. As time progresses, the mode (1,1) correlates either positively or negatively with other modes. To quantify the correlation between the flow modes during a flow reversal, we have computed the cross-correlation coefficient, $\mathrm{CC} = \overline{\hat{v}_{(m,n)} \cdot \hat{v}_{(1,1)}}/[\mathrm{RMS}(\hat{v}_{(m,n)})\mathrm{RMS}(\hat{v}_{(1,1)})]$, where $\cdot$ is the inner product and the overline is the time average computed within the flow reversal. The CC ranges between -1 (negatively correlated) and $+1$ (positively correlated). If $\mathrm{CC} = 0$, then change associated with the mode (1,1) is not felt by

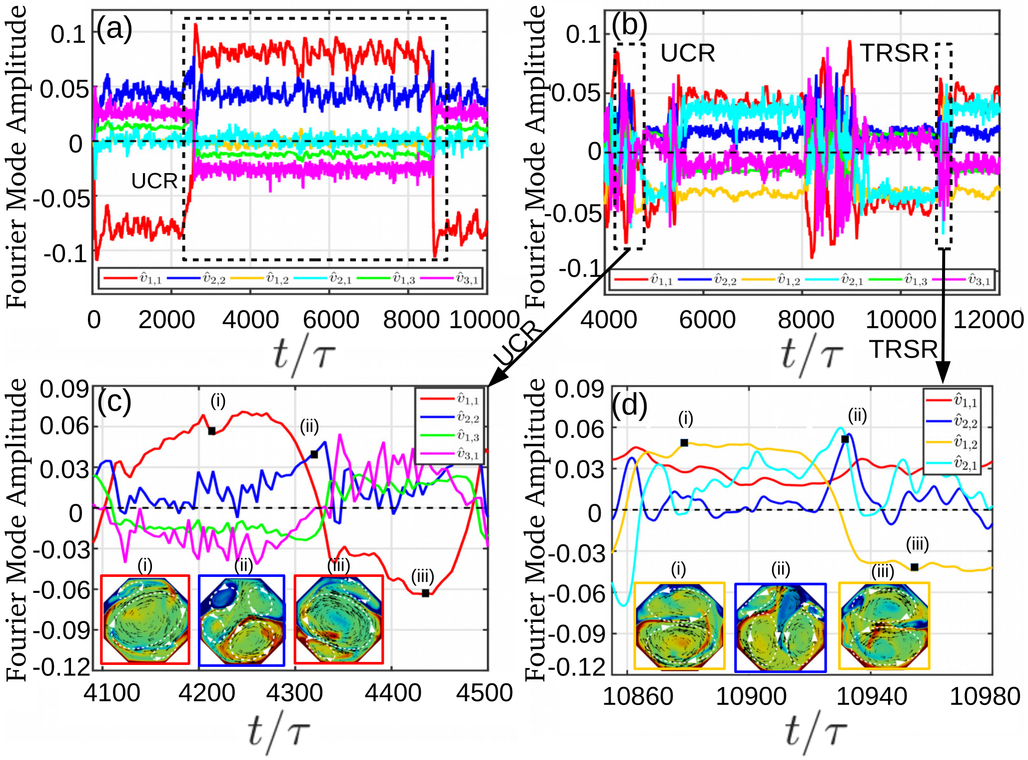

FIG. 8. The Fourier mode amplitude vs time: (a) $\alpha = 0^\circ$ in the UCR state and (b) $\alpha = 45^\circ$ in combined UCR+TRSR state. Dashed rectangular boxes in panels highlight flow mode features. Zoomed views of panel (b) are shown in panels (c) and (d), along with corresponding flow fields. Simulations are for Ra $= 10^8$ and Pr $= 1.8$.

the mode (m, n). Note, the CC reveals only the statistical connection between the modes, whereas the mode amplitude (or strength) reveals the dominant flow structure at a given instant of time. In Fig. 9(b) we have shown CC versus α. In a square enclosure ($\alpha = 0^\circ$), the corner-roll growth leads to the LSC breakup, so the quadrupole mode (2,2) correlates negatively with the mode (1,1). The dipole mode (2,1) correlates positively with the monopole, whereas the mode (1,2) does not correlate. The other modes (1,3) and (3,1) are correlated negatively with the monopole mode (1,1) mode. With an increase in α, the negative correlation of the quadrupole mode (2,2) decreases significantly, and we have observed CC ≈ 0 at $\alpha = 45^\circ$. With an increase in α, the dipole mode (1,2), which does not correlate with the monopole mode (1,1) in a square enclosure, correlates negatively, and, thus, a competition between the modes (1,2) and (1,1) takes place. The other modes (1,3) and (3,1) always show negative correlation with the mode (1,1). The modes (1,3) and (3,1) play a negligible role in flow reversals due to the strong dipole mode (1,2). A summary of flow patterns and their mode nature is mentioned schematically in the Appendix; see Fig. 30.

V. FLOW-REVERSAL FREQUENCY

Sugiyama *et al.* [15] have shown flow reversals in a 2D square (or quasi-2D) enclosure in the range $5 \times 10^6 \leqslant \text{Ra} \leqslant 10^9$ and $0.8 \leqslant \text{Pr} \leqslant 10$ are driven by the growth of counterrotating corner rolls. Wang *et al.* [38] had shown reversals are possible in a thin vertical circular enclosure when the corner rolls were absent. Recently, Chen *et al.* [40] have shown that flow reversals can be possible

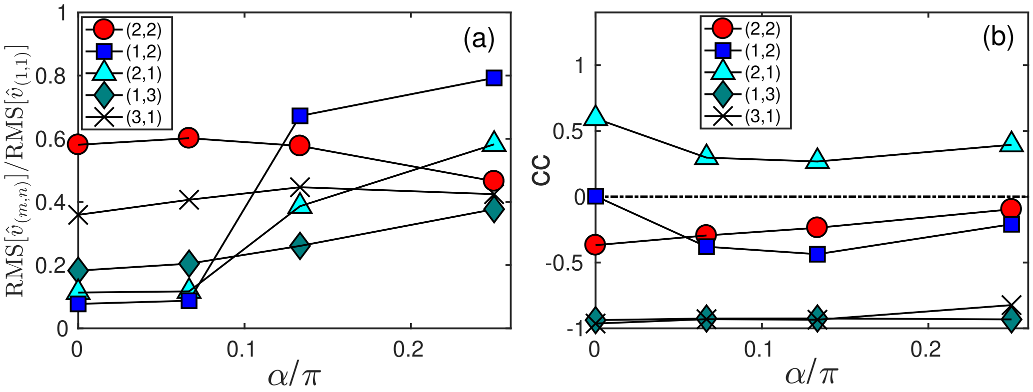

FIG. 9. Comparison of the Fourier mode amplitudes: (a) $\mathrm{RMS}[\hat{v}_{(m,n)}]/\mathrm{RMS}[\hat{v}_{(1,1)}]$ vs α, and (b) cross-correlation coefficient (CC) between $\hat{v}_{(m,n)}$ mode and $\hat{v}_{(1,1)}$ mode. Symbols: circles for (2,2) mode, squares for (1,2) mode, triangles for (2,1) mode, diamonds for (1,3) mode, and crosses for (3,1). Simulations are for $\mathrm{Ra} = 10^8$ and $\mathrm{Pr} = 1.8$.

due to instability of the LSC in addition to the corner-roll growth process. In a square enclosure for $\mathrm{Pr} = 5.7$, the dimensionless flow-reversal frequency follows a power-law relation in the form $ft_E \propto \mathrm{Ra}^{-1.08}$ for $1.18 \times 10^8 \leqslant \mathrm{Ra} \leqslant 2 \times 10^8$, and $ft_E \propto \mathrm{Ra}^{-2.83}$ for $2 \times 10^8 < \mathrm{Ra} \leqslant 1.12 \times 10^9$ [40]. By arranging additional slanted adiabatic plates at the four corners of the square enclosure, in the form of an octagon (see geometric construction in the Ref. [40]), the reversal frequencies show $ft_E \propto \mathrm{Ra}^{-1.53}$ for $2 \times 10^8 < \mathrm{Ra} \leqslant 3.71 \times 10^8$ and $ft_E \propto \mathrm{Ra}^{-5.05}$ for $2 \times 10^8 < \mathrm{Ra} \leqslant 3.71 \times 10^8$ for $\mathrm{Pr} = 5.7$. From Ref. [40], we can observe that the flow-reversal frequency decreases in an enclosure with the adiabatic slanted walls. The absence of corner-roll growth is the reason attributed to the decrease in flow-reversal frequency. Note, the mentioned power-law scalings in Ref. [40] are limited in range.

In our work, we have used slanted conduction walls (instead of adiabatic walls) in four corners of the square enclosure; see Fig. 1(b). For $\mathrm{Ra} < 10^7$, the flow reversals take place by an alternate ejection of mushroom-shaped plumes from the slanted walls. For $\mathrm{Ra} > 10^7$, the reversals take place by both the corner-roll growth and the two-roll state [see Fig. 8(b) and Fig. 32 in the Appendix]. To compute the flow-reversal frequency, we have used the angular momentum (L) signal. We denote the start time of a reversal by t_s [black square marker symbols in Fig. 5(a)] and the end time of a reversal by t_e [black circle marker symbols in Fig. 5(a)]. The time interval between two successive reversals n and $n+1$ is computed as $t_{int} = t_s(n+1) - t_e(n)$. We have considered the mean reversal frequency as $f = 1/\bar{t}_{int}$. In Fig. 10 we have shown the mean reversal frequency as a function of Ra for different α and compared our results with the previous findings of Refs. [15,39,40,46]. From the figure, we can note that the dimensionless reversal frequency decreases with an increase in Ra, similar to Refs. [15,46]. The small difference between our work and the mentioned other works can be due to variation in Pr. For $\mathrm{Ra} \leqslant 10^8$, the reversal frequency follows, $ft_E \propto \mathrm{Ra}^{\phi}$, where $\phi \approx -0.358$ for $\alpha = 0^\circ$ (red dashed line) and $\phi \approx -0.281$ for $\alpha = 45^\circ$ (cyan dashed line). From our simulations, we can infer that the flow-reversal frequency increases with an increase of α. Note, the flow-reversal frequencies and the associated modes highly depend on the location on the Ra-Pr flow map. We have also computed the reversal frequencies separately for the UCR and the TRSR states when both the flow states coexist; see Fig. 31 in the Appendix. In the octagonal enclosure, both the UCR and the TRSR states strengthen with an increase in α, and, thus, the flow-reversal frequencies are high. We have shown f versus α for different Ra in the inset of Fig. 10. The frequency increases linearly with an increase of α. The linear slope varies from 1.04 to 0.328 as Ra increases from 5×10^5 to 10^8, respectively. For very high Ra (i.e., $>10^9$) Araujo *et al.* [35] have modeled a single plume detachment from the boundary layers in terms of the force and thermal energy balance on a single

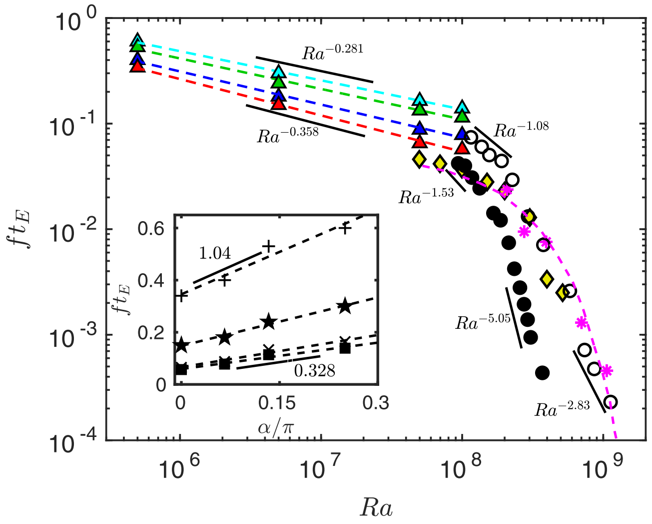

FIG. 10. Dimensionless flow-reversal frequency (ft_E) as a function of Ra on a log-log plot. Open black circles for experiments in quasi-2D square cell with Pr = 5.4 [39], which follow $ft_E \sim \mathrm{Ra}^{-1.08}$ in the range $1.18 \times 10^8 \leqslant \mathrm{Ra} \leqslant 2 \times 10^8$, and follow $ft_E \sim \mathrm{Ra}^{-2.83}$ in the range $2 \times 10^8 < \mathrm{Ra} \leqslant 1.12 \times 10^9$. Filled black circles for experiments in quasi-2D cornerless cell with Pr = 5.4 [40], which follow $ft_E \sim \mathrm{Ra}^{-1.53}$ in the range $9.58 \times 10^7 \leqslant \mathrm{Ra} \leqslant 2 \times 10^8$. Yellow diamonds for numerical data of Sugiyama *et al.* [15] at Pr = 4.3. Magenta asterisks for experimental data of Ni *et al.* [46] at Pr = 5.7. Magenta dashed line approximately fits the magenta asterisks and is obtained from stochastic model proposed by Brown and Ahlers [50]. Our numerical data at Pr = 2 are shown as upward triangles: Red for $\alpha = 0^\circ$, blue for $\alpha = 12^\circ$, green for $\alpha = 24^\circ$, and cyan for $\alpha = 45^\circ$. We have shown best power-law fits of our data with dashed lines. Red dashed line for $\alpha = 0^\circ$ follows $ft_E \sim \mathrm{Ra}^{-0.358}$, and cyan dashed line for $\alpha = 45^\circ$ follows $ft_E \sim \mathrm{Ra}^{-0.281}$. In the inset, we have shown ft_E vs α/π, where plus, pentagram, cross, and square symbols are for $\mathrm{Ra} = 5 \times 10^5$, 5×10^6, 5×10^7, and 10^8, respectively. Inset shows the reversal frequency scales linearly with an increase in α. The corresponding linear slopes are shown above the best fits. The eddy turnover time (t_E) decreases from 40τ to 15τ as Ra increases from 10^5 to 10^8, respectively, which is consistent with the results of Ref. [55,56].

plume, for which the reversal frequency increases with Ra in the range $10^9 < \mathrm{Ra} < 10^{12}$. From our results and from the experiments of Ref. [40], we can note that a single plume description may be a simplified approximation to describe the flow reversals. In the next section, we have explored the heat transport dynamics.

VI. EFFECT ON HEAT TRANSPORT

Heat transport in thermal convection depends on Ra and Pr and on the geometry [58,59]. The dimensionless heat transport in a system is quantified by the Nusselt number, $\mathrm{Nu}(t) = 1 + \langle v(T - T_m)\rangle/(\kappa \Delta T/H)$, where $\langle \cdot \rangle$ is the total area average in the 2D enclosure. We have also separately calculated the Nusselt number based on the wall thermal gradients $\mathrm{Nu}(t)|_{h,c} = [-k \iint \frac{\partial T}{\partial \mathbf{n}} \cdot \mathbf{n}\, dl]|_{h,c}/[kl\Delta T/H]$, where $\mathbf{n}$ is the unit vector normal to the conduction wall, dl is the infinitesimal conduction wall length, l is the total conduction wall length (which can be either hot or cold), and $|_{h,c}$ represents the thermal gradient computed at the hot and the cold walls, respectively. The average Nusselt number based on the wall gradients is taken as $\mathrm{Nu}(t) = \frac{1}{2}[\mathrm{Nu}(t)|_h + \mathrm{Nu}(t)|_c]$. In our work, the difference in the Nusselt numbers based on the convective flux and the thermal wall gradients is less than 0.3%. We have shown the time averages in the statistically stationary state by an overline.

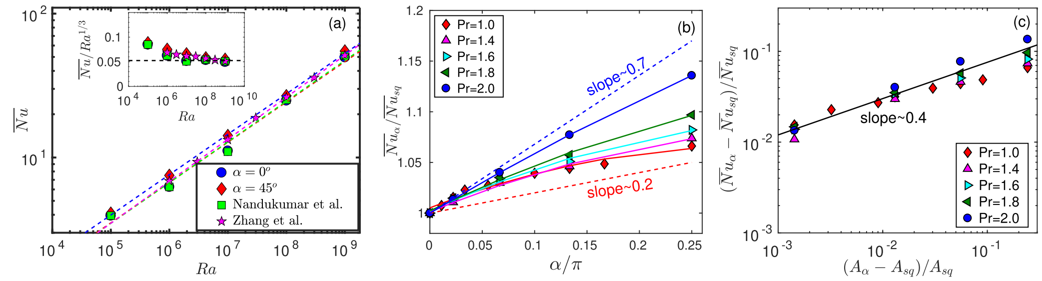

FIG. 11. (a) $\overline{\mathrm{Nu}}$ vs Ra: blue circles for square ($\alpha = 0^\circ$) and red diamonds for octagon enclosure ($\alpha = 45^\circ$) at Pr = 1. Green squares for Ref. [44] at Pr = 1. Magenta stars for Ref. [57] at Pr = 5.3. Dashed lines to guide the eye. (b) $\overline{\mathrm{Nu}}_\alpha/\overline{\mathrm{Nu}}_{sq}$ vs α/π. Continuous lines are best least-square fits in the form $Y = aX^2 + bX + c$, where $X = \alpha/\pi$, and $Y = \overline{\mathrm{Nu}}_\alpha/\overline{\mathrm{Nu}}_{sq}$. The fit parameters range is $-0.65 \leqslant a \leqslant -0.31$, $0.39 \leqslant b \leqslant 0.63$, and $c = 1$. Dashed lines represent a linear trend along with their corresponding slopes. (c) Effective increase in Nusselt number vs increase in wall conduction area of the octagon. (b) and (c) Simulations of Ra = 10^8 and different Pr. Symbols are red diamonds (Pr = 1), magenta upward triangles (Pr = 1.4), cyan rightward triangles (Pr = 1.6), green leftward triangles (Pr = 1.8), and blue circles (Pr = 2.0).

Between a square and an octagonal enclosure, which one is better in terms of high heat transport? To address this, in Fig. 11(a) we have shown $\overline{\mathrm{Nu}}$ versus Ra for $\alpha = 0^\circ$ and 45°. We find the octagonal enclosures show high heat transport (up to 14% increase) when compared to the square cell. In the inset of the same figure, we have shown $\overline{\mathrm{Nu}}/\mathrm{Ra}^{1/3}$ as a function of Ra. Based on the best power-law fit, we can approximate the heat transport in the form $\overline{\mathrm{Nu}} \sim \mathrm{Ra}^\gamma$, where $0.29 \leqslant \gamma \leqslant 0.31$ in the range $10^7 \leqslant \mathrm{Ra} \leqslant 10^8$ for both square and the octagonal enclosures. The scaling exponent γ is consistent with earlier findings on heat transport [14,17,44,60].

In Fig. 11(b) we have shown the relative heat transport $\overline{\mathrm{Nu}}_\alpha/\overline{\mathrm{Nu}}_{sq}$ as a function of α, where $\overline{\mathrm{Nu}}_{sq}$ and $\overline{\mathrm{Nu}}_\alpha$ are the time-averaged Nusselt numbers for the square and the octagonal enclosures, respectively. Our numerical data follow $Y = aX^2 + bX + c$, where $X = \alpha/\pi$ and $Y = \overline{\mathrm{Nu}}_\alpha/\overline{\mathrm{Nu}}_{sq}$. The parameters a, b, and c are in a range $-0.65 \leqslant a < -0.31$, $0.39 \leqslant b < 0.63$, and $c = 1$, based on the best quadratic fits. The lower bounds in the mentioned fit parameters are for Pr = 1, and the upper bounds are for Pr = 2. Additionally, we have shown two dash lines with linear slopes 0.2 and 0.7, which pass through the data point ($\alpha = 0^\circ$ and $\overline{\mathrm{Nu}}_\alpha = \overline{\mathrm{Nu}}_{sq}$), to indicate the lower and upper limits on the heat transport.

It is natural to expect that the dimensional heat transport is high in the octagonal enclosure due to an increase in wall conduction length when compared to the square cell. However, we have presented our results based on dimensionless heat transport, i.e., the Nusselt number, which has already taken care of the increase in wall conduction length (or area in 3D). For example, when we calculate the Nusselt number based on the thermal gradients at the wall, the integral in the numerator is compensated by the total conduction length in the denominator. So any increase in the Nusselt number (or the dimensionless heat transport) is not due to the increase in the wall conduction area. In Fig. 11(c) we have shown percentage increase in the Nusselt number $[(\overline{\mathrm{Nu}}_\alpha - \overline{\mathrm{Nu}}_{sq})/\overline{\mathrm{Nu}}_{sq}]$, as a function of percentage increase in conduction area $[(A_\alpha - A_{sq})/A_{sq}]$. From the figure, we can note that a power-law scaling with an exponent 0.4 governs the relative heat transport dynamics. The mentioned power-law scaling is a statistical fit to the data and does not have any physical basis. However, it is interesting to note that for an increase in the conduction area, the Nusselt number does not increase proportionately. The scaling relation may have practical relevance in choosing better engineering designs.

Though, the scaling exponent γ is nearly the same for both the square and the octagonal enclosures; still, the instantaneous heat transport, Nu(t), is very different. For $\alpha > 6^\circ$, the heat transport shows intense fluctuations when compared to the square cell. The slanted conduction walls

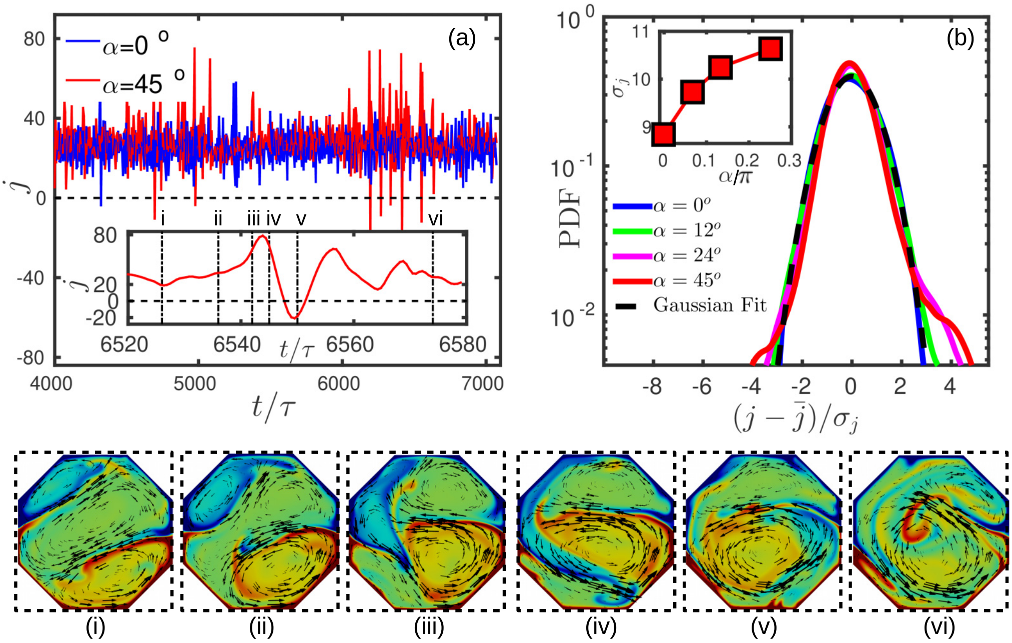

FIG. 12. (a) Convective heat flux (j) vs time for $\alpha = 0^o$ (blue) and 45° (red). In inset, zoomed view of j with time during a flow reversal. Vertical dashed lines indicate times at which six snapshots of the velocity and temperature fields are taken. The snapshots are timed at (i) $t = 6526\tau$, (ii) 6536τ, (iii) 6542τ, (iv) 6545τ, (v) 6550τ, and (vi) 6574τ. The flow-reversal process is described as (i) and (ii) for growth of corner rolls; (iii) for corner-roll reconnection; (iv) for flow reconfiguration; (v) for hot plumes falling and cold plumes rising; and (vi) for hot plumes rising and cold plumes falling. (b) PDFs of normalized convective heat flux $(j - \overline{j})/\sigma_j$. Blue line is for $\alpha = 0^\circ$, green for 12°, magenta for 24°, and red for 45°. The normal Gaussian is represented by long dashed lines. The standard deviation (σ_j) vs α is shown in inset of panel (b). Simulations for $\mathrm{Ra} = 10^8$ and $\mathrm{Pr} = 2$.

of the octagonal enclosure provide easy access for the heat to enter the fast-moving large-scale circulation. To understand the connection between the flow states on the heat transport, we have computed dimensionless convective heat flux in the enclosure, $j(t) = \langle v(T - T_m)/(\kappa \Delta T/H)\rangle$, as a function of time; see Fig. 12(a). The fluctuations in $j(t)$ indicate rising and falling plume motions. Whenever the hot (cold) plumes get trapped in the down-falling (uprising) motions, we observe negative j, and the large-scale motion ceases to exist [17]. In the inset of Fig. 12(a) we have shown a zoomed view of the heat flux and the associated thermal fields for the octagonal enclosures. The standard deviation (σ_j) increases from 9 to 11 with an increase in α; see the inset of Fig. 12(b). For the square enclosure, $\overline{j} \approx 25$ and $\sigma_j \approx 0.36\overline{j}$, whereas we find $\overline{j} \approx 28.5$ and $\sigma_j \approx 0.37\overline{j}$ at $\alpha = 45^\circ$. In both cases, the standard deviation is more than 36% of the mean value, and such high values for σ_j indicate the presence of turbulent fluctuations. The probability density functions (PDFs) of the normalized heat flux $(j - \overline{j})/\sigma_j$ are shown in Fig. 12(b). The PDFs are non-Gaussian at the tails and show intermittency.

In a 2D enclosure, the aspect ratio $\Gamma = D/H$, is defined as a ratio between the conduction wall length and the separation distance between the hot and the cold walls; see Fig. 1 for the notation. For a square enclosure, $D = H$, and hence $\Gamma = 1$. For a wider enclosure, $\Gamma > 1$, whereas, for a taller enclosure, $\Gamma < 1$. In the case of an octagonal enclosure, a single aspect ratio definition is not appropriate, because both the conduction wall length and the distance of separation depend on the spatial location. For example, in the case of $\alpha = 12^\circ$, the total conduction wall length (either the hot

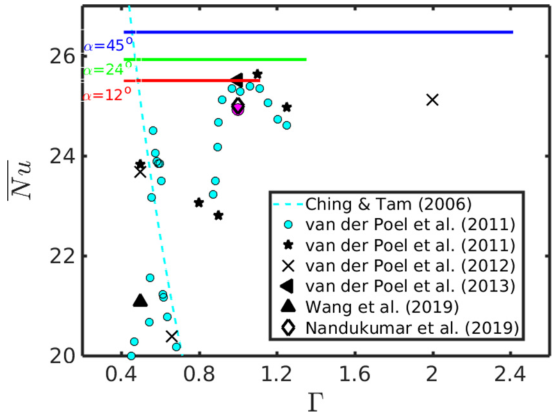

FIG. 13. $\overline{\mathrm{Nu}}$ (time-averaged Nusselt number) dependence on Γ in 2D thermal convection. For $\mathrm{Ra} = 10^8$, $\mathrm{Pr} = 1$ and $\Gamma = 1$, we find $\overline{\mathrm{Nu}} = 24.89$ from our simulations (see magenta circle), which agrees with the results of Ref. [44] (open black diamond). We have also collated data from other works to understand Γ dependence and show these data: cyan dashed line from Ref. [62]; cyan circles from Ref. [23] for $\mathrm{Ra} = 10^8$ and $\mathrm{Pr} = 0.7$; black stars from Ref. [23] for $\mathrm{Ra} = 10^8$ and $\mathrm{Pr} = 4.3$; black crosses from Ref. [24] for $\mathrm{Ra} = 10^8$ and $\mathrm{Pr} = 1$; black leftward triangle from Ref. [61] for $\mathrm{Ra} = 10^8$ and $\mathrm{Pr} = 4.38$; and black upward triangle from Ref. [54] for $\mathrm{Ra} = 10^8$ and $\mathrm{Pr} = 0.71$. Our numerical data for the octagonal enclosures are shown with continuous lines: red for $\alpha = 12^\circ$, green for $\alpha = 24^\circ$, and blue for $\alpha = 45^\circ$. Note, for a given α, we have a $\overline{\mathrm{Nu}}$ and a range of aspect ratios with a lower limit and an upper limit (which are connected by a horizontal line).

or the cold wall) is $1.013H$, and the insulated (adiabatic) wall length is $0.8754H$. Based on these wall lengths, we get $\Gamma = 1.013H/0.875H = 1.1571 > 1$. If the aspect ratio is computed based on the horizontal conduction wall length (by excluding the slanted walls) and the maximum distance of separation between the walls, then $\Gamma = 0.414H/H = 0.414$. So the actual aspect ratio for $\alpha = 12^\circ$ enclosure varies between 0.414 and 1.1571. Based on the α value, the minimum and the maximum limits of the aspect ratio of the octagonal enclosure changes, thus there is no unique aspect ratio definition. The earlier works on the RB convection highlighted the importance of the aspect ratio in terms of the multiple flow states and the heat transport [24,61], so we have explored further details in that regard.

In Fig. 13 we have shown $\overline{\mathrm{Nu}}$ as a function of Γ, in which data from various thermal convection studies are mentioned [23,24,44,61,61–63]. Ching and Tam [62] proposed that $\propto f(\Gamma)$, where the function $f(\Gamma)$ decreases monotonically with Γ (see cyan dash line in the same figure). Van der Poel *et al.* [23,24] explored the aspect ratio dependence on the heat transport by using 2D simulations and found sudden jumps in $\overline{\mathrm{Nu}}$. A noteworthy observation from the earlier works is that a maximum $\overline{\mathrm{Nu}}$ is observed at $\Gamma \approx 1.1$. For the octagonal enclosures, a single aspect ratio is not possible, and hence, we have drawn a continuous line that joins the minimum and the maximum aspect ratio limits (as discussed earlier). For example, we have shown a red horizontal line ranges from $\Gamma = 0.414$ to 1.1571 at $\overline{\mathrm{Nu}} = 25.3$ and $\alpha = 12^\circ$. Similarly, we have drawn a horizontal line in green from $\Gamma = 0.414$ to 1.4 at $\overline{\mathrm{Nu}} = 25.8$ and $\alpha = 24^\circ$. We have also drawn a blue line from $\Gamma = 0.414$ to 2.4 at $\overline{\mathrm{Nu}} = 26.5$ and $\alpha = 45^\circ$. Our results clearly show that the octagonal enclosures transport more heat when compared to the square cell.

In our simulations, at $\alpha = 0^\circ$, the corner rolls trap most of the thermal plumes and thus thick thermal boundary layers near the corners. With an increase in α, the importance of the quadrupole mode (2,2) decreases, and the dipole emerges as a dominant flow feature. Indeed, the dipole mode (1,2) helps in achieving better flow circulation in the octagonal enclosure; see animation 4 in the Supplemental Material [45]. In Figs. 14(a)–14(f) we have shown time-averaged temperature fields for $\alpha = 0^\circ$, 24°, and 45°. At $\mathrm{Ra} = 10^7$ and $\mathrm{Pr} = 1$, in a square enclosure, we find a stable

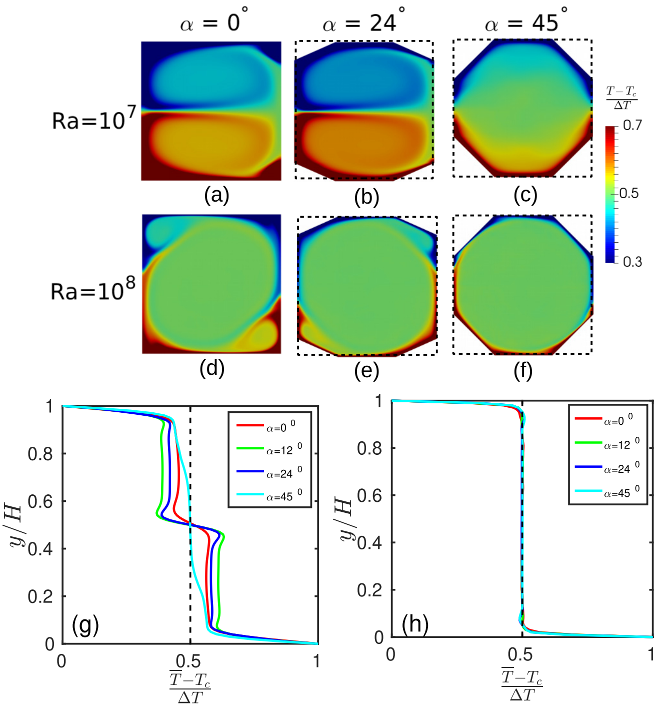

FIG. 14. Long-time-averaged temperature fields for more than 7000τ: Top panels (a, b, and c) for $\mathrm{Ra} = 10^7$, and bottom panels (d, e, and f) for $\mathrm{Ra} = 10^8$. Panels (a) and (d) for $\alpha = 0^\circ$, panels (b) and (e) for $\alpha = 24^\circ$, and panels (c) and (f) for $\alpha = 45^\circ$. Color bar for dimensionless temperature, $(\overline{T} - T_c)/\Delta T$, in the range 0.3 (blue) to 0.7 (red). Time-averaged temperature profile along the vertical midline of the enclosure: panel (g) for $\mathrm{Ra} = 10^7$ and panel (h) for $\mathrm{Ra} = 10^8$. Thermal gradient at the walls increases with increase in α. Simulations for $\mathrm{Pr} = 1$.

dipole state. With an increase in α, the combined UCR and the TRSR states replace the dipole. In Figs. 14(g) and 14(h) we have shown time-averaged temperature profiles taken along the vertical midline in the enclosure. We can note that the time-averaged thermal gradient at the walls increases with an increase of α.

In Fig. 15(a) we have shown time-averaged thermal gradient computed normal ($\mathbf{n}$) to the hot wall, i.e., $\nabla\overline{T} \cdot \mathbf{n}$, for three different α. Note, the wall-normal gradient varies along the conduction wall. In the square enclosure, the wall gradient is a direct function of x, the horizontal coordinate. The octagonal enclosure consists of inclined conduction walls in addition to the horizontal walls. So we have first computed the wall-normal gradient at each point on the conduction wall and shown the result as a function of the corresponding x coordinate. In a square enclosure, the gradient is high in the midportion of the conduction wall between $0.3D < x < 0.7D$, and it is low near the left and right corner portions. Within the simulation time limits, we found the large-scale circulations are asymmetric in shape about the midline of the enclosure, and that leads to the nonuniform thermal gradient on the conduction walls. For $\alpha = 45^\circ$, the dipole mode strongly shears the flow, and the corner rolls move freely, which result in nearly uniform thermal gradient on the conduction wall. In Fig. 15(b) we have shown the wall-length averaged thermal gradient, $\overline{\xi} = \frac{1}{l_i}\int \nabla\overline{T} \cdot dl_i$, as a function of α. Here the integration is carried out along a particular wall l_i, which can be the left slanted wall, the middle horizontal wall, or the right slanted wall. With an increase in α, the heat transport decreases at the middle wall and increases at the slanted walls. The additional buoyancy provided by the slanted walls is the reason for the observed increase in heat transport.

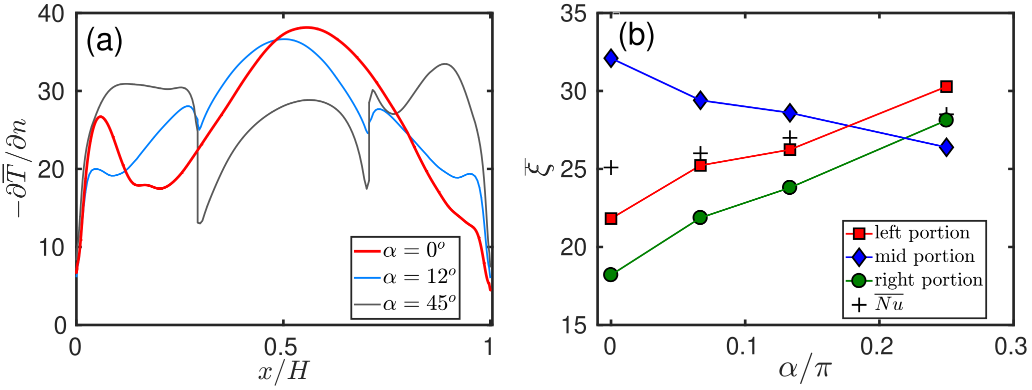

FIG. 15. (a) Wall thermal gradients measured normal to the bottom conduction walls ($\nabla\overline{T}\cdot\mathbf{n} = \frac{\partial\overline{T}}{\partial n}$) for $\alpha = 0^\circ$, 12°, and 45°. (b) Wall-length-averaged thermal gradient ($\overline{\xi} = -\frac{1}{l_i}\int\nabla\overline{T}\cdot dl_i$) for the left, right, and the middle (horizontal) conduction walls. Here l_i is the length of a particular conduction wall. The plus symbols in panel (b) show $\overline{\mathrm{Nu}}$ as a function of α. Simulations for $\mathrm{Ra} = 10^8$ and $\mathrm{Pr} = 2$. We have considered time averages from 500τ to $15\,000\tau$ with a time gap of 50τ to compute wall thermal gradients. Within this time average, we did not observe the expected left-right symmetry in wall-thermal gradient on the conduction wall.

VII. THE TURBULENT MECHANICAL ENERGY BUDGET TO UNDERSTAND PLUME ENGULFMENT INTO THE BULK REGION

From the earlier section, we have observed that heat transport increases with an increase of α. In general, either by increasing the flow circulation over the conduction walls or by inducing turbulence, one can increase the convective motions in the enclosure. In a square RB convection for $\mathrm{Ra} \leqslant 10^7$, the plumes rise or fall on the enclosure (square) walls, and they rarely penetrate the core bulk region. For $\alpha > 12^\circ$, we have observed the thermal plumes engulfed into the core bulk zone; see animation 5(a–d) in the Supplemental Material [45]. To understand thermal plume engulfment into the bulk core region, we have computed the turbulent mechanical energy budget at a relatively high Rayleigh number, $\mathrm{Ra} = 10^8$. Inspired by the Fourier mode analysis, we have separated the flow information into two separate zones: Zone I and the Zone II; see Fig. 1. The chosen zone partition is not entirely arbitrary. From the Fourier mode analysis, we can note these zones capture the large-scale modes very well. First, we have computed various flow quantities such as the kinetic energy, local buoyancy force, local probe information of the velocity, and the temperature fields. The probe information clearly shows intense fluctuations in the core bulk region. Further, we have computed the local vorticity and the Richardson numbers to understand the importance of the buoyancy in the different zones. Finally, we have calculated the turbulent energy budget to understand the transport mechanism to explain the thermal plumes' engulfment into the core bulk region.

A. Zone-area-based kinetic energy in the flow

We have computed the zone-based average kinetic energy (per unit mass) in the flow as $E_{\mathrm{kin}}(t) = \frac{1}{2A_Z}\iint_{A_Z}\mathbf{u}\cdot\mathbf{u}\,dx\,dy$, where $\iint_{A_Z}$ is the area integral chosen separately in Zone I and Zone II. In Figs. 16(a) and 16(b) we have shown E_{kin} versus time for two different α, in comparison to the square enclosure. In both Zones I and II, E_{kin} shows fluctuations with the time. The rising and falling motions near the sidewalls in the square enclosure set the high kinetic energy in the Zone II region. With an increase in α, a strong dipole circulation emerges in the enclosure, and the kinetic energy increases in both Zones I and II; see Fig. 16(c). For $\alpha > 12^\circ$, the inertial forces in the core bulk region become important, and thus the kinetic energy in Zone I is more than in Zone II. Later, we show that in Zone I, hydrodynamic instabilities arise due to the plume ejections from the slanted walls.

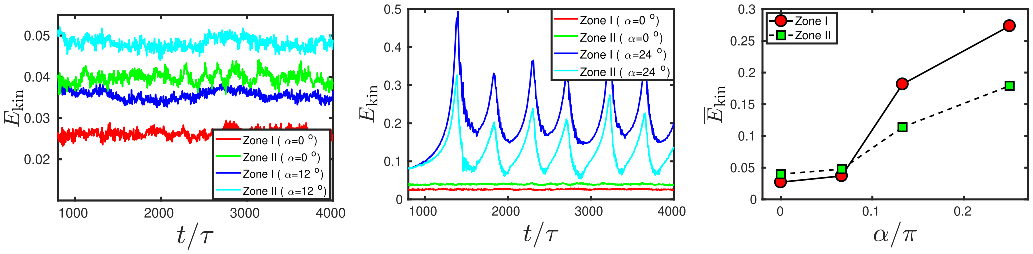

(a)

(b)

(c)

FIG. 16. Panels (a) and (b) for zone-area-averaged instantaneous kinetic energy per unit mass (E_{kin}) vs time. We have compared Zone I and Zone II information of the octagonal enclosures with the square enclosures. In panel (c), time-averaged kinetic energy ($\overline{E}_{\text{kin}}$) as a function of α. Note, Zone I for core bulk region and Zone II for near wall shear layers. Symbols are circles (for Zone I) and squares (for Zone II). Note, the kinetic energy is normalized with $\kappa^2 \text{Ra}\,\text{Pr}/H^2$ to make it dimensionless. Simulations for $\text{Ra} = 10^8$ and $\text{Pr} = 1$.

In Fig. 17 we have shown time series of the velocity and the temperature fluctuations taken at three different probe locations. In the figure, the first row is for the horizontal velocity (u), the second row is for the vertical velocity (v), and the third row is for the temperature. We have chosen three probes, $P1$, $P2$, and $P3$, outside the thermal boundary layers to track transport process between the zones; see Fig. 1. For example, the time-averaged temperature profile along the midline of the enclosure, i.e., $\overline{T}(x = H/2, y = 0)$, is a useful measure to estimate the thermal boundary layer thickness, δ_{DNS}. From our simulations, we have computed the thermal gradient at the hot conduction walls from the time-averaged temperature profile and then estimated the thermal boundary layer thickness as $\delta_{\text{DNS}} = [T_H - T_m]/|\frac{\partial T}{\partial y}|_{wall}$. Note, the thermal boundary layer thickness estimation varies locally along the conduction walls, and the midline based estimation which we have taken is a reasonable choice. In the square RB convection, $\delta_{\text{DNS}} \approx 0.02$ based on midline temperature profile

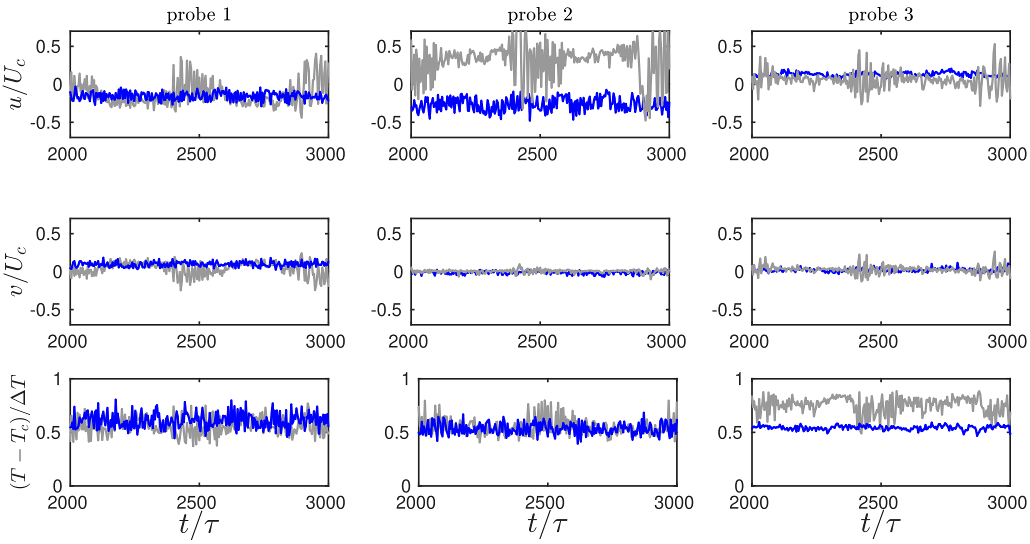

FIG. 17. Time series of velocity and temperature at probe $P1$, probe $P2$, and probe $P3$ locations. Probe locations can be noted from Fig. 1. Top row for horizontal velocity, middle row for vertical velocity, and bottom row for temperature. Dark blue lines for $\alpha = 0^\circ$ and light gray lines for $\alpha = 24^\circ$. Simulations for $\text{Ra} = 10^8$ and $\text{Pr} = 1$.

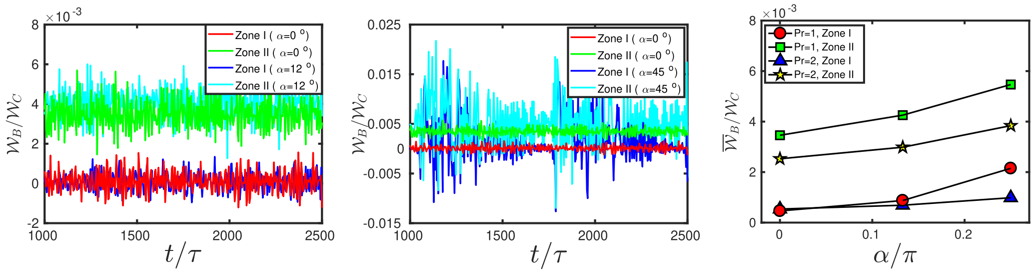

(a) (b) (c)

FIG. 18. Zone-area-averaged instantaneous work done by buoyancy $\mathcal{W}_B$. Panels are for (a) $\alpha = 12^\circ$ and (b) $\alpha = 45^\circ$ in comparison to a square RB convection ($\alpha = 0^\circ$). Panel (c) is for time-averaged work done by buoyancy ($\overline{\mathcal{W}}_B/\mathcal{W}_C$). Here $\mathcal{W}_C = \rho_m \beta \Delta T |g| U$. Symbols are circles (for Zone I and Pr = 1), squares (for Zone II and Pr = 1), triangles (for Zone I and Pr = 2), and stars (for Zone II and Pr = 2). Simulations are for $\mathrm{Ra} = 10^8$.

at $\mathrm{Ra} = 10^8$ and $\mathrm{Pr} = 1$, and the estimate is within 0.6% (error) mentioned in earlier work [44]. In the octagonal enclosure, the boundary layer thickness decreases due to an increase in the dipole circulation, so the chosen probe locations can track the transport exchanged into the core bulk region. In the case of RB convection, the large-scale monopole generates a strong wind sweep and the probe $P2$ detects a high value of horizontal velocity, whereas the vertical component of velocity is nearly zero. The probes $P1$ and $P3$, are relatively far from the wall boundary layers in the square enclosure, whereas they are somewhat near the slanted conduction walls in the octagonal enclosure (but still in the core bulk zone). With an increase of α, the wind strengthens, and thus we see an intense flow at probe $P1$ and $P3$. The increase in velocity fluctuations in the core bulk region indicates an increase in the nonlinear (or the advective) motions.

B. Work done by buoyancy

In thermal convection, buoyancy plays an important role by driving local fluid. To understand further, we have explored work done by the buoyancy by taking the dot product between the velocity and the buoyancy terms. In the mechanical energy balance, the buoyancy term acts as a source, the viscous term acts as a sink, and the other terms such as the advection and the pressure terms redistribute the energy in the flow. Moreover, the energy balance terms act differently in the core bulk region and the boundary layers. We have computed the zone area-averaged work done by the buoyancy as $\mathcal{W}_B = \frac{1}{A_Z} \iint_{A_Z} \rho_m \beta (T - T_m) \mathbf{g} \cdot \mathbf{u} \, dx \, dy$. For $\mathcal{W}_B > 0$, the hot plumes rise and the cold plumes sink, whereas for $\mathcal{W}_B < 0$, the hot plumes sink and the cold plumes rise. For $\mathcal{W}_B > 0$, the temperature field acts as an active scalar and drives the flow; otherwise, the fluid drives the passive temperature field. In Fig. 18 we have shown $\mathcal{W}_B$ versus time. Zone I mainly consists of turbulent fluctuations with intermittent bursts of plumes, and hence, $\mathcal{W}_B$ fluctuates around zero. In Zone II we observe many rising and falling thermal plumes [64] and the time average $\overline{\mathcal{W}}_B > 0$. With an increase in α ($> 12^\circ$), the buoyancy work increases considerably in both the zones; see Figs. 18(b) and 18(c). It is noteworthy mentioning that the buoyancy work (when compared to the kinetic energy) increases with α.

C. The origin of instability in the bulk core region and the local Richardson number

In convection, thermal energy enters the conduction walls and generates a wide range of large and small scales of motion. From the phenomenological models [11], we can note that the mechanical energy drains out at the walls by the laminar shear and by the turbulent fluctuations in the core bulk region; thus, heat transport mechanism in these two zones are very different by nature. The thermal plume ejections from the boundary layers and their interaction with the core bulk region further complicate the transport process [65]. Even, if we consider a single thermal parcel (like a simplified fluid blob), which has exceeded a certain threshold in the temperature difference with the calm surroundings, we can set complex convective motions [13]. What happens to the parcel if it somehow enters a turbulent environment which shows a wide range of spatiotemporal motions? The parcel may rise unsteadily, or it may be broken into smaller plumes and mix up with the local fluid. In a closed enclosure, the mentioned scenarios of thermal plume motion highly depend on the interplay between the buoyancy, the wall shear motions and the turbulent engulfments from the core. Especially in the octagonal enclosures, the slanted conduction walls assist the plumes in providing additional buoyancy. In convection, the Richardson number ($\mathrm{Ri}_{\mathrm{local}}$), which is defined as a ratio of the buoyancy production to the shear production, i.e., $\mathrm{Ri}_{\mathrm{local}} = [|\mathbf{g}|\,\frac{\partial \rho}{\partial y}]/[\rho_0|\frac{\partial u}{\partial y}|^2]$, is a good measure for knowing the driving mechanism. Here ρ is the local density (which depends on the temperature), and u is the velocity component in the wind direction. The Richardson number is another way of comparing the required buoyancy to the resulting nonlinearity in the flow [13]. In the case of turbulent atmospheric convection, the local Richardson number (sometimes called the flux Richardson number) is defined based on the ratio of the time-averaged production by the buoyancy to the production by the Reynolds shear stress, $\mathrm{Ri}_{\mathrm{flux}} = [|\mathbf{g}|\overline{\rho' u_i' \delta_{ij}}]/[-\rho \overline{u_i' u_j'} \frac{\partial \overline{U}_i}{\partial x_j}]$, where $'$ are the fluctuation quantities, indices i and j vary in the coordinate directions, δ_{ij} is the Kronecker delta, and uppercase letters are the mean flow information. For $\mathrm{Ri}_{\mathrm{flux}} \gg 1$, the flow is statistically stable; otherwise, the flow ultimately shows hydrodynamic instabilities [66]. For $\mathrm{Ri}_{\mathrm{flux}} = 1$, the mechanical production rate balances the buoyancy flux, thus the marginal stability. Laminar flow cannot maintain its stability if $\mathrm{Ri} < 0.25$, whereas a turbulent flow (may) relaminarizes if $\mathrm{Ri} \gg 1$ (with hysteresis effects). Though the critical (or the cutoff) values are always subject to intense research, we can note that small values of the Richardson number based on either local or the fluxes) correspond to an increase in random fluctuations (or nonlinear effects) in the flow. Note, in a fully developed turbulent flow $\mathrm{Ri}_{\mathrm{flux}}$ is a better choice as a measure, whereas $\mathrm{Ri}_{\mathrm{local}}$ is suitable when such restrictions are unknown prior.

Vincent and Yuen [67] have conducted 2D numerical simulations with stress-free boundary conditions in the large aspect ratio ($\Gamma = 3$) enclosure for $\mathrm{Ra} = 10^8$ and $\mathrm{Pr} = 1$. In their work, the local Richardson number is defined as $\mathrm{Ri}_{\mathrm{RBC}} = |\mathbf{g}|\beta\frac{\partial \theta}{\partial y}/(\frac{\partial u}{\partial y})^2$, where $\theta = [T(x, y) - \overline{T}(y)]$ is the thermal anomaly with respect to the linear conduction state $\overline{T}(y)$. Based on $\frac{\partial \theta}{\partial y}$, we may have a stable, or a marginally stable, or unstable environment in the enclosure. For $\mathrm{Ri}_{\mathrm{RBC}} < 0.25$, the thermal anomalies promote local mixing and generate small-scale thermal plumes from the boundaries with an inversion in a local temperature gradient [67]. In our simulations, the convective motions are weak due to small $\mathrm{Ra}(\leqslant 10^8)$, compared to strong turbulent motions expected at a relatively high $\mathrm{Ra}(\geqslant 10^{14})$. In that case, $\mathrm{Ri}_{\mathrm{local}}$ (which is equivalent to $\mathrm{Ri}_{\mathrm{RBC}}$ under the Boussinesq approximation) is an excellent measure to quantify buoyancy to the shear-based motion. Any small values of $\mathrm{Ri}_{\mathrm{RBC}}$ may create horizontal inversion layers; thus, there is a possibility of internal waves with baroclinic instabilities. The other way to understand the instabilities and their growth is by computing the local vorticity levels in the flow. In thermal convection, by taking the curl of the momentum equation, we get the vorticity transport equation,

$$\frac{\partial \Omega}{\partial t} + \underbrace{\mathbf{u} \cdot \nabla \Omega}_{\text{Advection}} = \underbrace{-|\mathbf{g}|\beta\frac{\partial T}{\partial x}}_{\text{Baroclinic torque normal to } xy \text{ plane}} + \underbrace{\nu \nabla^2 \Omega}_{\text{Viscous}}, \tag{5}$$

where $\Omega = \nabla \times \mathbf{u}$ is the vorticity. In our 2D simulations, the vorticity acts normal to the xy plane. In Eq. (5) the baroclinic torque acts as a source to drive the flow from the conduction state. With time, the vorticity either gets amplified or redistributed in the flow, whereas the viscosity diffuses it. The excess generation of vorticity increases the nonlinear effects and, thus, the flow instabilities.

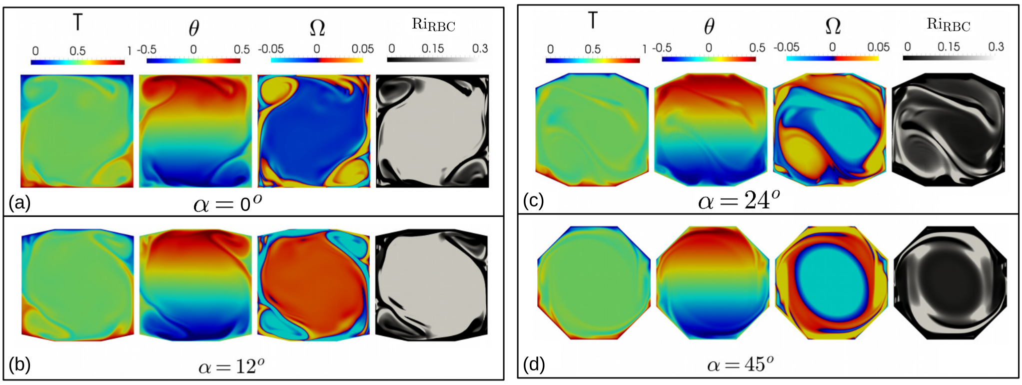

FIG. 19. In each panel: first column for instantaneous thermal field (T), second column for thermal anomaly (θ), third column for vorticity (Ω), and fourth column for local Richardson number ($\mathrm{Ri}_{\mathrm{RBC}}$). Panels are for $\alpha =$ (a) 0°, (b) 12°, (c) 24°, and (d) 45°. Simulations are for $\mathrm{Ra} = 10^8$ and $\mathrm{Pr} = 1$ at time $t = 2400\tau$. See animation 5(a–d) in the Supplemental Material [45] for more details.

With the above discussion in mind, in Fig. 19 we have shown instantaneous contours of the temperature (T), the thermal anomaly (θ), the vorticity (Ω), and the local Richardson number ($\mathrm{Ri}_{\mathrm{RBC}}$). In the case of a square RB convection ($\alpha = 0^\circ$), we have observed a relatively uniform temperature (with $T \approx T_m$) in the core bulk region (or Zone I) with a stratified thermal anomaly without any fluctuations. In Zone I we found $\mathrm{Ri}_{\mathrm{RBC}} \gg 0.3$ and the vorticity $|\Omega| \leqslant 10^{-4}$, which indicate a stable monopole. The thermal anomaly and its fluctuations are visible near the conduction walls and in the corner rolls. In Zone II the buoyancy effects are strong, and the local vorticity is high, i.e., $|\Omega| \approx 0.05$. There the local Richardson numbers are much smaller than 0.1, which indicate the growth of corner rolls. In contrast, with an increase of α, both Zone I and II show intense fluctuations in the thermal anomaly. Notably, we observe local $\mathrm{Ri}_{\mathrm{RBC}} < 0.25$ in Zone I for $\alpha > 12^\circ$. In the octagonal enclosures, the quadrupole mode can freely move from the corners without being pinned at a fixed location. Due to the dipole mode, high values of vorticity and velocity fluctuations develop in the enclosure. From animation 5(a–d) in the Supplemental Material [45], we can note that turbulent-like engulfments take place from Zone II to Zone I.

In Fig. 20 we have shown area-averaged vorticity transport as a function of time. For $\alpha < 12^\circ$, both the baroclinic torque and the viscous diffusion balance each other. With a further increase in $\alpha(>12^\circ)$, hydrodynamic instabilities are triggered in the core bulk zone. At high $\mathrm{Ra}(>10^7)$, the vorticity transport terms show vigorous fluctuations with time, and hence, we have quantified their intensity in terms of the root-mean-square (RMS) values; see Fig. 21. With an increase in α, both the baroclinic torque and the viscous term increase linearly with a slope of 0.18. The advection, which is small in comparison to the other terms, increases significantly for $\alpha > 24^\circ$ and becomes a dominant term. We have used the least-square linear fit procedure to compute the slopes, and the statistical errors involved are less than ±0.05 in slope. Based on this evidence, we can infer that an increase in the advection terms leads to the plume engulfments into the Zone I region.

D. Mechanical energy budget

To understand the engulfment mechanism mentioned earlier, we have computed the turbulent kinetic energy budget in the enclosure. First, we briefly revisit the earlier works on turbulence studies. In the isothermal turbulence studies in three dimensions, the supplied mechanical energy at the large scales transfers via the intermediate scales and finally dissipates by the molecular

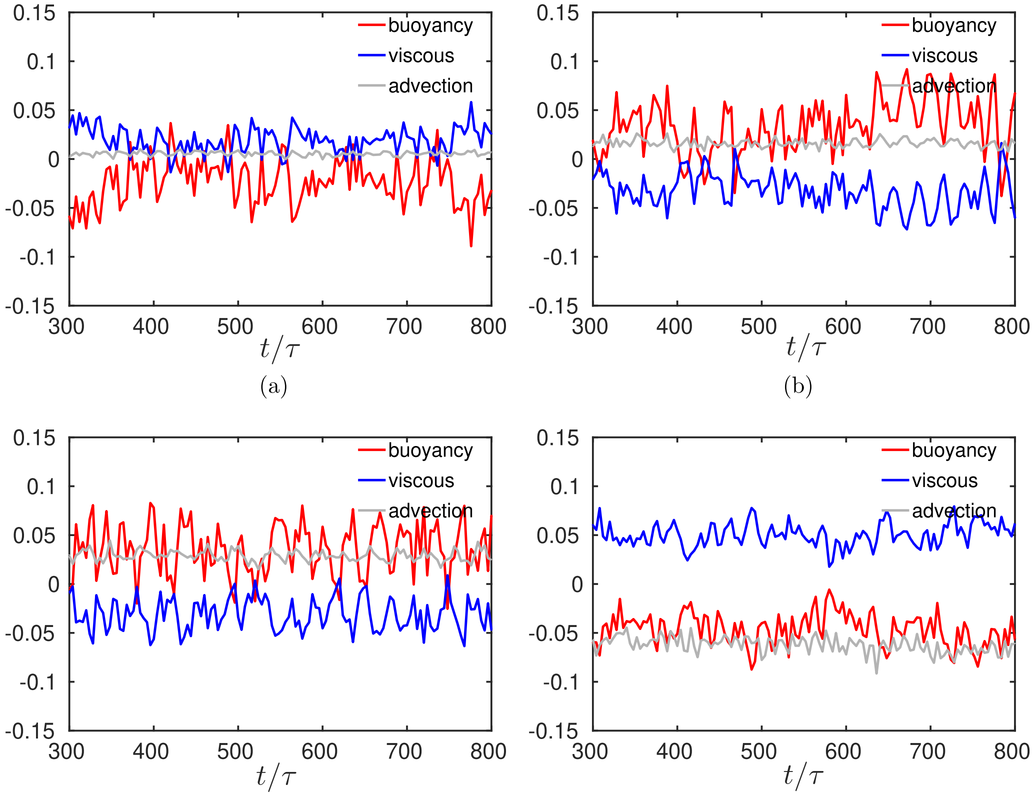

(a) (b) (c) (d)

FIG. 20. Area-averaged vorticity transport terms such as the buoyancy ($|\mathbf{g}|\beta\frac{\partial T}{\partial x}$), the viscous ($\nu\nabla^2\Omega$), and the advection ($\mathbf{u}\cdot\nabla\Omega$) terms as functions of time. Panels are for (a) $\alpha = 0^\circ$, (b) 6°, (c) 12°, and (d) 24°. Note, the terms are area averaged and normalized by U^2/H^2 to make them dimensionless. Simulations are for $\mathrm{Ra} = 10^8$, $\mathrm{Pr} = 1$.

viscosity [21]. In the case of RB convection, thermal potential energy enters at the conduction walls instead of the kinetic energy and drives the flow. The thermal boundary layers interact with the core bulk region, and that leads to occasional plume detachments and the convective motions [11]. Some of the phenomenological studies of RB convection [10,12,68], have attempted to estimate the total heat transport by partitioning the fluid layers in the enclosure into a turbulent core bulk region, the wall shear boundary layers, and perhaps additional intermediate mixing zones [65]. From a phenomenological point of view [68], the kinetic energy dissipation of each zone is different, and the statistics in these zones show complex spatiotemporal variation in the form of laminar mushroom plumes, sheetlike plumes, and random fluctuations; see more details in Refs. [69–75]. Recent works by Petschel *et al.* [76], indicate that the dynamical zone information based on the energy dissipation is more appropriate when compared to the classical boundary layer based information. Also, the transport mechanisms in the 2D and the 3D studies are different [21].

It is a common practice in turbulent flows to decompose any instantaneous field, such as the velocity $\mathbf{u}$, the pressure p, and the temperature T, into a sum of mean flow and fluctuations, i.e., $\mathbf{u} = \overline{\mathbf{U}} + \mathbf{u}'$, $p = \overline{P} + p'$, and $T = \overline{T} + T'$, where the overline $\overline{(\cdot)}$ is the time average and $(\cdot)'$ is the fluctuation. The turbulent kinetic energy (TKE) budget which governs the fluctuations [21] is

$$\frac{\partial(ke)}{\partial t} = C_K + P_K + T_K + D_K + \epsilon_K + \Pi_K + B_K, \tag{6}$$

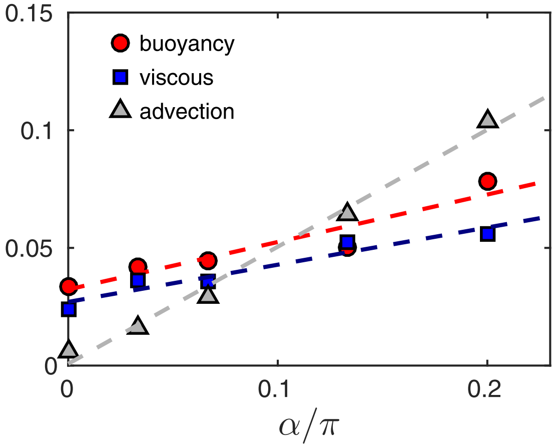

FIG. 21. Root-mean-square (RMS) values of vorticity terms vs α. Symbols shown for buoyancy (circles), viscous (squares), and advection (triangles) terms. The advection terms increase significantly for $\alpha > 12^\circ$. Dashed lines are best linear fits. Simulations for $\mathrm{Ra} = 10^8$ and $\mathrm{Pr} = 1$.

where $ke = \frac{1}{2}u'_i u'_i$ is the turbulent kinetic energy, $P_K = -\overline{u'_i u'_j}\frac{\partial \overline{U}_i}{\partial x_j}$ is the shear production by the Reynolds stresses, $T_K = -\frac{1}{2}\frac{\partial}{\partial x_j}(\overline{u'_i u'_i u'_j})$ is the turbulent transport, $C_K = -\frac{1}{2}\overline{U}_j\frac{\partial}{\partial x_j}(\overline{u'_i u'_i})$ is the convective transport, $D_K = \frac{1}{2}\nu\frac{\partial^2}{\partial x_j \partial x_j}(\overline{u'_i u'_i})$ is the transport by the viscosity, $\epsilon_K = -\nu\overline{\frac{\partial u'_i}{\partial x_j}\frac{\partial u'_i}{\partial x_j}}$ is the viscous dissipation, $\Pi_K = \overline{u'_i \frac{\partial p'}{\partial x_i}}$ is the velocity-pressure gradient term, and $B_K = |g|\beta\overline{T' u'_i}\delta_{ij}$ is the buoyancy production term. The indices i and j are varied in both the horizontal and vertical directions. In Fig. 22 we have shown isocontours of the RMS fluctuations developed in thermal convection. The spatial inhomogeneity in the velocity and the temperature fluctuations indicate that the momentum transport is quite different in the wall boundary layers and the turbulent core bulk region. Due to the large-scale motions, the vertical velocity near the horizontal walls and the horizontal velocity near the vertical walls show high values in magnitude. With an increase of α ($> 12^\circ$), the RMS fluctuations increase significantly, and the temperature fields become more homogeneous.

The turbulence production in thermal convection takes place by both the shear (P_K) and the buoyancy (B_K) terms. The Reynolds shear stress terms contribute via P_K, whereas the convective terms contribute via B_K. In Fig. 23 we have shown instantaneous contours of both P_K and B_K terms. In the square enclosure, the turbulence production takes place via P_K near the corner rolls, and via B_K, at the thermal plume clusters [77]. In the octagonal enclosures, with an increase in α, both P_K and B_K increase and show complex spatial dependence. The shear-driven motions and the buoyancy-driven plume clusters can be seen even in the core bulk region of the octagonal enclosures. The P_K terms show both the positive and the negative fluctuations, which indicate that the local turbulent energy exchanges from the mean to the fluctuations and vice versa. However, the total area-averaged P_K is always be zero in the enclosure, supporting that the fluctuations do not cross the enclosure walls. The area-averaged B_K is always positive, and it increases with an increase of α. The total area-averaged B_K is at least an order of magnitude larger than P_K. In the core bulk region of the square enclosure, both the P_K and B_K are negligibly small; thus, we observe a stable monopole. However, the production terms increase significantly in the octagonal enclosure contributing to the observed hydrodynamic instabilities. To quantify the overall energy budget, mainly in the Zone I, we have computed an area and time-averaged individual budget terms as a function of α; see Fig. 24. As explained earlier, the area-averaged buoyancy production dominates the core region dynamics compared to the total shear production. Thus the observed hydrodynamic instabilities in Zone I and the turbulent engulfments across Zone I and Zone II.

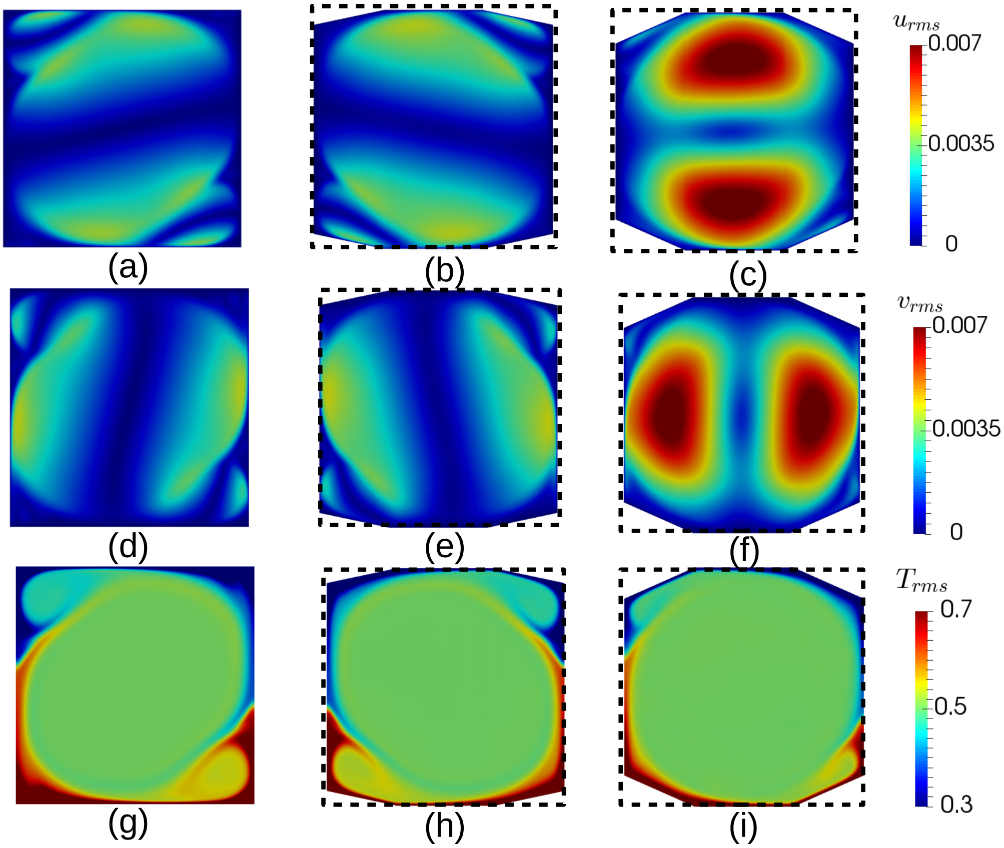

FIG. 22. Isocontour plots of time-averaged RMS fluctuations: (a–c) for horizontal velocity, (d–f) for vertical velocity, and (g–i) for temperature. Left panels for $\alpha = 0^\circ$, middle panels for $\alpha = 12^\circ$, and right panels for $\alpha = 24^\circ$. Note, color bars range differently in each panel. In each row, $\alpha = 0^\circ$, 12°, and 24° are shown. Simulations are for $\mathrm{Ra} = 10^8$ and $\mathrm{Pr} = 1$.

VIII. SUMMARY AND CONCLUSIONS

To investigate the importance of the corner rolls, which are assumed to be the primary reason for the flow reversals in two-dimensional (2D) thermal convection, in our work, we have probed

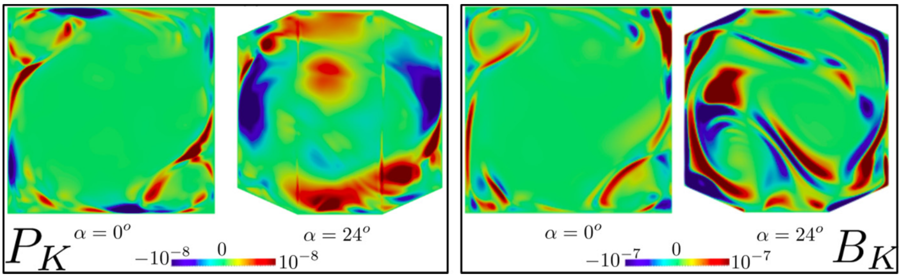

FIG. 23. Instantaneous isocontours of turbulent production terms: left panels for shear production (P_K), and right panels for buoyancy production (B_K). In each panel, results for $\alpha = 0^\circ$ and $\alpha = 24^\circ$ are shown. Note, color bar ranges differently in each panel. Simulations are for $\mathrm{Ra} = 10^8$ and $\mathrm{Pr} = 1$.

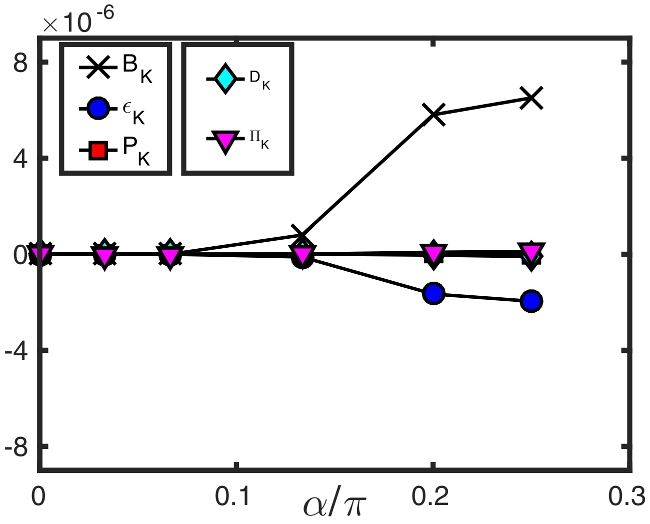

FIG. 24. Time- and area-averaged mechanical energy budget terms in the turbulent core bulk region (Zone I) as functions of α. Symbols are crosses (B_K), circles (ϵ_K), squares (P_K), diamonds (D_K), and downward triangles (Π_K). Simulations for $\mathrm{Ra} = 10^8$ and $\mathrm{Pr} = 1$.

a geometry in the form of an octagonal enclosure inscribed in a square (see Fig. 1). Similar to the classical Rayleigh-Bénard convection, we have maintained the left-right symmetry in thermal boundary conditions and the no-slip in velocity on the enclosure walls. We have studied flow features and heat transport in the octagonal enclosure by varying the slanted wall angle (α) from 0° to 45°, in the parameter range $5 \times 10^5 \leqslant \mathrm{Ra} \leqslant 10^8$ and $0.8 \leqslant \mathrm{Pr} \leqslant 2.0$. In the square enclosure (for which $\alpha = 0°$), the corner rolls exchange thermal energy with the conduction walls, grow with time, and are stably arrested in motion by the enclosure edges. Due to the vortex reconnection mechanism, the corner rolls merge and induce flow reversals with an intermediate state in the form of a uniform circulation. In the case of an octagonal enclosure, the slanted conduction walls supply additional heat to the corner rolls, and a robust dipole mode develops due to frequent plume ejections from the slanted walls. At low Ra ($< 10^7$), the mushroom-shaped plume ejections take place alternatively from the slanted walls and the flow set into periodic and quasiperiodic reversals. At high Ra ($\geqslant 10^8$), turbulent engulfments take place from the wall zones, and hydrodynamic instabilities arise in the core bulk region.

We have quantified the overall flow features as a result of the competition between various Fourier modes and traced the flow map on the Ra-Pr plane for different α (see Figs. 3 and 6). With an increase in α, the contribution by the quadrupole mode decreases and the dipole mode increases, which highlights that the corner rolls are not essential to explain the flow-reversal mechanism in 2D thermal convection. We have found that the energy contribution by the dipole increases from 5% (for $\alpha = 0°$) to 80% (for $\alpha = 45°$) at $\mathrm{Ra} = 10^8$. The flow-reversal frequency increases linearly with α and decreases as a power law with Ra. The normalized mean flow-reversal frequency is proportional to Ra^{ϕ}, where ϕ varies from -0.358 at $\alpha = 0°$ to -0.281 at $\alpha = 45°$. At high Ra ($= 10^8$), with an increase in α, the core bulk region shows a combination of both the monopole and the dipole states with frequent flow reversals. The core bulk region shows intense fluctuations in both velocity and temperature. To probe reasons for these hydrodynamic instabilities, we have carried out a turbulent energy budget by considering two different zones: the wall zone and the core bulk zone. We have observed turbulent-like engulfments between the wall and the core bulk zones due to high shear production (P_K) term. The engulfed plumes easily penetrate the core bulk zone and release their thermal energy by the buoyancy production (B_K) term. With an increase in α, the overall convective motions increases, which results in high heat transport (up to 14% increase) when compared to the square enclosure. The observed increase in heat transport mainly comes from the slanted conduction walls when compared to the contribution from the horizontal conduction walls. For $\alpha > 24^\circ$, the advective motions dominate, and the slanted walls release many thermal plumes to the bulk core, and thus high heat transport.

In conclusion, we recommend an octagonal enclosure (with $\alpha = 45^\circ$) as a better choice to achieve excellent thermal mixing and high heat transport compared to a square enclosure. Any further geometry variation, slanted wall angles, or more complicated boundary conditions can be work for future scope.

ACKNOWLEDGMENTS

Our sincere thanks to Prof. Mahendra K. Verma and his group members at IIT Kanpur for the invaluable discussions and providing us with their computational code. We acknowledge the anonymous referees for showing us the correct direction by asking questions and helping us to improve the manuscript. We thank the Computational Mechanics Group members, IIT Kharagpur, for their help in preparing the manuscript. We acknowledge the financial support and computational resources provided by the Department of Science and Technology, Government of India, through Innovation in Science Pursuit for Inspired Research (INSPIRE), and the Board of Research Nuclear Sciences (BRNS), Department of Atomic Energy, Government of India. R.L. acknowledges the Param Shakti-National Supercomputing Mission, Government of India for providing their computational resources.

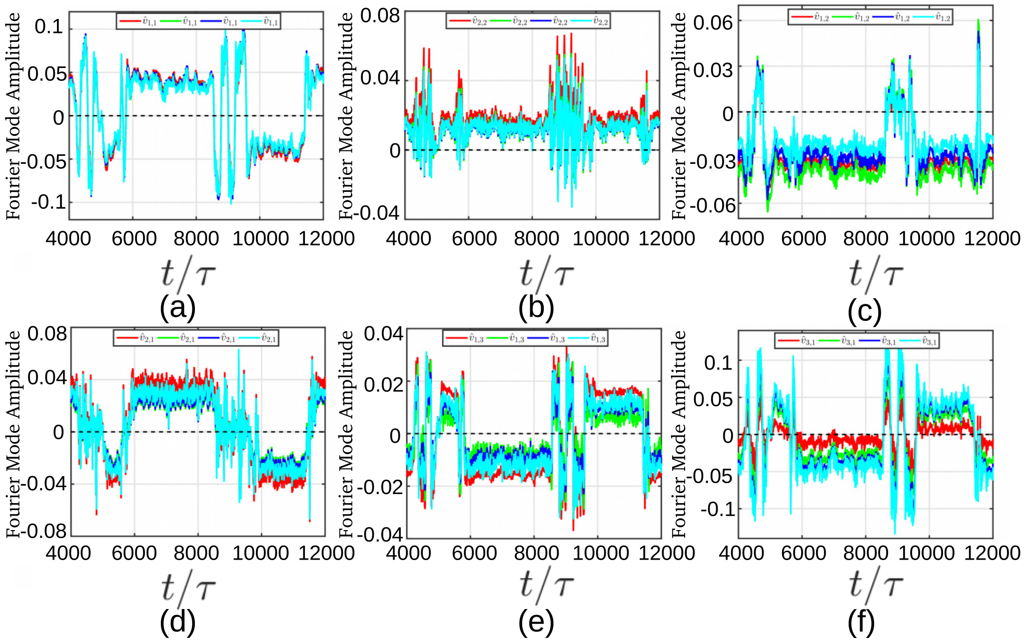

(a) (b) (c) (d) (e) (f)

FIG. 25. Fourier mode decomposition is carried out for the vertical velocity in the three subdomains. Lines are green (for the green square domain), blue (for the blue square domain), and cyan (for the cyan square domain). In each panel, a particular Fourier flow mode amplitude as a function of dimensionless time is shown: (1,1) mode (a), (2,2) mode (b), (1,2) mode (c), (2,1) mode (d), (1,3) mode (e), and (3,1) mode (f). The mode amplitudes from the complete octagon domain (without separating it into square domains) are shown as a red line. Simulations for $\mathrm{Ra} = 10^8$, $\mathrm{Pr} = 1.8$, and $\alpha = 45^\circ$ enclosure.

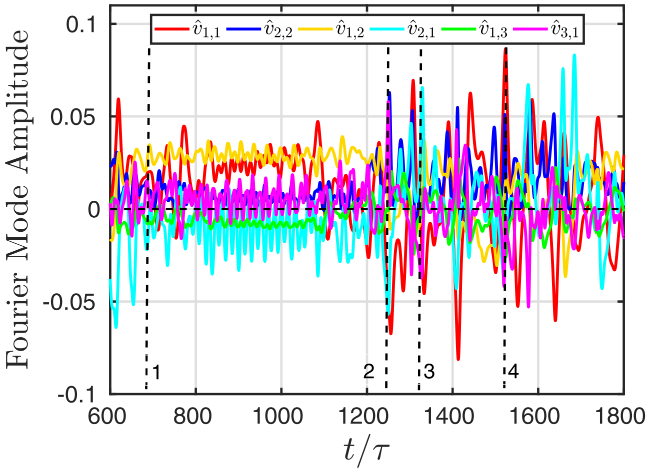

FIG. 26. Time evolution of the dominant Fourier modes for square enclosure at Ra = 5×10^5 and Pr = 2. At 1, 2, 3, and 4 we have shown dashed lines for which four snapshots are shown in Fig. 3(a).

APPENDIX

In this Appendix, we have supplemented the paper with additional details on flow reversals.

In Fig. 25 we have shown six dominant Fourier modes: (1,1) in (a), (2,2) in (b), (1,2) in (c), (2,1) in (d), (1,3) in (e), and (3,1) in (f) for the mentioned three square subdomains; see Fig. 1(b). The mode amplitude shows a similar trend for all three subdomains. Also, we have computed Fourier modes for the complete octagon domain, and the resulting amplitude variation follows the same trend, suggesting that the considered square subdomains are sufficient to capture the large-scale information. With these inferences, we have computed the Fourier mode decomposition in the blue square subdomain ($0.2D \leqslant x \leqslant 0.8D$ and $0.2H \leqslant y \leqslant 0.8H$), and based on that, we have shown our results in the paper.

We have shown the Fourier mode amplitudes for the mixed state with reversals (MSR) for the square enclosure ($\alpha = 0^\circ$) in Fig. 26 as an extension of Fig. 3. Here 1 represents two-roll structure,

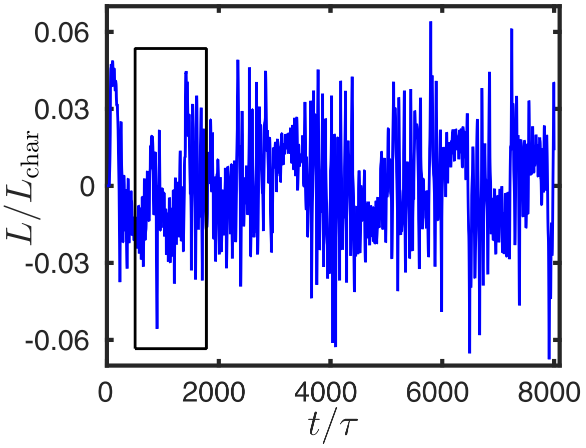

FIG. 27. Normalized angular momentum vs time for mixed state with reversal (MSR) in a square enclosure for the parameters Ra = 5×10^5 and Pr = 2. Zoom of rectangular box shown in Fig. 3.

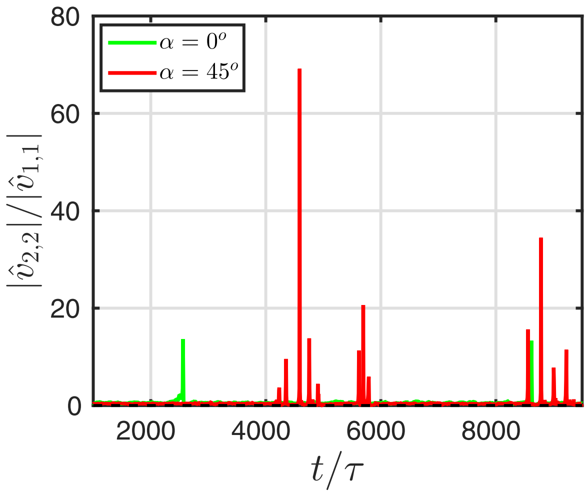

FIG. 28. The ratio of $|\hat{v}_{2,2}|/|\hat{v}_{1,1}|$ for Ra $= 10^8$ and Pr $= 1.8$ for $\alpha = 0^\circ$ (green) and $\alpha = 45^\circ$ (red).

2 and 3 represent a mixed state, and 4 represents uniform circulation, which is reconfirmed by analyzing the Fourier mode amplitudes: the (1,2) mode is dominant in 1; (2,1), (3,1), and (2,2) show a spike in 2 and 3; and (1,1) mode is dominant in 4. In the MSR case, there is no special order of different flow states such as UC, TRS, and some other complex flow states.

In Fig. 27 we have shown the relatively long signal of angular momentum versus time for MSR in a square enclosure for Ra $= 5 \times 10^5$ and Pr $= 2$. The black rectangular portion represents the zoomed view shown in Fig. 3(b).

During the UCR, the mode (1,1) crosses zero and the mode (2,2) shows a spike. The disappearing of the (1,1) mode and the spike in the (2,2) mode are responsible for four rolls appearing during the reversal. In Fig. 28 we have shown the the ratio $|\hat{v}_{2,2}|/|\hat{v}_{1,1}|$ with time for Ra $= 10^8$ and Pr $= 1.8$. The UCR take place when $|\hat{v}_{2,2}|/|\hat{v}_{1,1}|$, shows a spike.

In Fig. 29 we have given a summary of the Fourier modes which are responsible (or interact mainly) during the flow reversal. For example, during the UCR, basic mode (1,1) changes its orientation due to growth of the (2,2) mode. In the case of TRSR, the basic mode (1,2) reorients due to growth of (2,2), which interacts with (2,1). In case of QPR, the basic mode is (1,1), which interacts in a major way with (2,2), (1,3), and (3,1) during reversal. In case of PR, the (1,1) mode interacts with (2,2), and (1,3) during reversal.

In Fig. 30 we have summarized information on flow states observed in the square and the octagon enclosures in the considered range of Ra and Pr. At high Ra $= 10^8$, the UC state, which

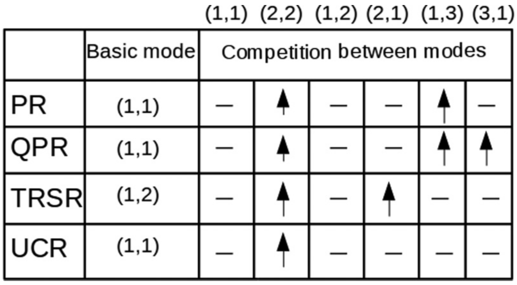

	Basic mode	Competition between modes					
		(1,1)	(2,2)	(1,2)	(2,1)	(1,3)	(3,1)
PR	(1,1)	–	↑	–	–	↑	–
QPR	(1,1)	–	↑	–	–	↑	↑
TRSR	(1,2)	–	↑	–	↑	–	–
UCR	(1,1)	–	↑	–	–	–	–

FIG. 29. Interaction between different Fourier modes during reversal. Upward arrow indicates significant influence of the specific modes.

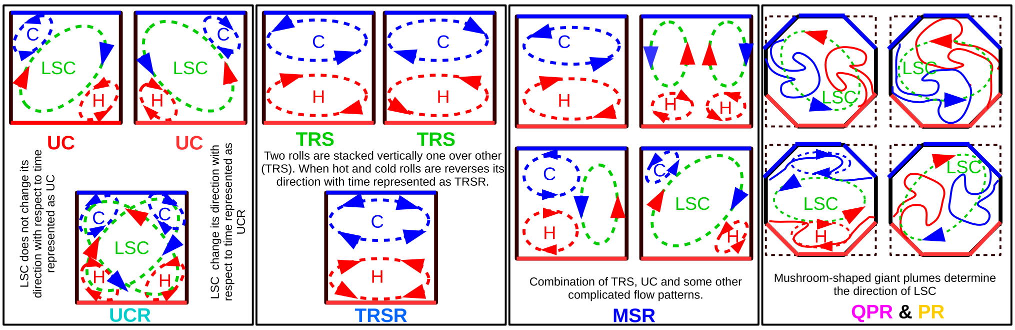

LSC does not change its direction with respect to time represented as UC

LSC change its direction with respect to time represented as UCR

Two rolls are stacked vertically one over other (TRS). When hot and cold rolls are reverses its direction with time represented as TRSR.

Combination of TRS, UC and some other complicated flow patterns.

Mushroom-shaped giant plumes determine the direction of LSC

FIG. 30. Schematics of different flow states observed in the given range of Ra-Pr. Note, hot (H) and cold (C) rolls and large-scale circulation (LSC). In QPR and PR, mushroom-shaped giant plumes eject from the incline walls.

is observed in both the square and octagon enclosures, consists of a large elliptical roll along with two small-scale counterrotating corner rolls. The large-scale uniform circulation (or the monopole) state becomes unstable due to growth of the corner rolls (or the quadrupole), which leads to the UCR state. During the flow reversal, the quadrupole mode (2,2) dominates over the monopole or the (1,1) mode. In the octagon enclosures, we have observed three additional flow states, namely, TRSR, MSR, and QPR and PR states, in addition to the UC, TRS, and UCR states. The TRS state, i.e., (1,2) mode, is observed for $\mathrm{Ra} \geqslant 10^7$ and $\mathrm{Pr} \geqslant 1$, where a cold roll lies above a hot roll in the stable state. The competition between (2,2) and (2,1) with the (1,2) mode leads to the flow reversals in the form of TRSR state. In the case of PR and QPR flow states, the monopole (1,1) mode is subjected to destabilize by the (2,2), (1,3), and (3,1) modes, which leads to reversals. In the MSR state, we have observed that the (1,1), (2,1), (1,2), (2,2), (3,1), and (1,3) modes occur randomly to trigger flow reversals.

In Fig. 31 we have shown normalized mean reversal frequency versus slanted angle for $\mathrm{Ra} = 5 \times 10^7$ and $\mathrm{Pr} = 2$. For a square enclosure ($\alpha = 0^\circ$) reversals can take place only by UCR, whereas

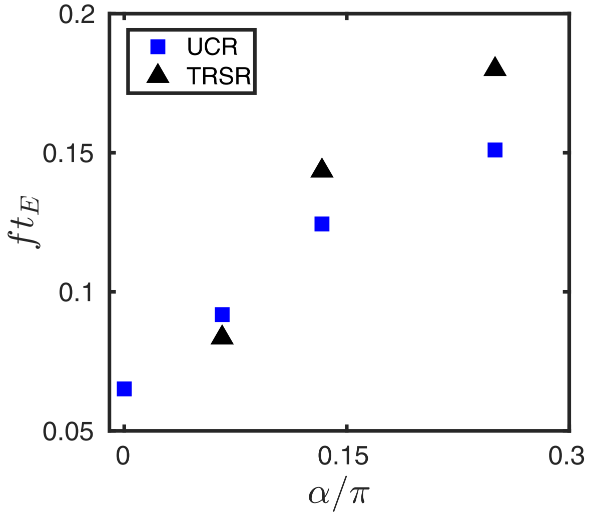

FIG. 31. Normalized mean reversal frequency vs slanted angle for $\mathrm{Ra} = 5 \times 10^7$ and $\mathrm{Pr} = 2$. For a square enclosure ($\alpha = 0^\circ$) flow reversals take place by UCR, and for $\alpha = 12^\circ$ to 45° case flow reversals take place by both UCR and TRSR. UCR is shown by a blue square, and TRSR is shown by black triangle symbols.

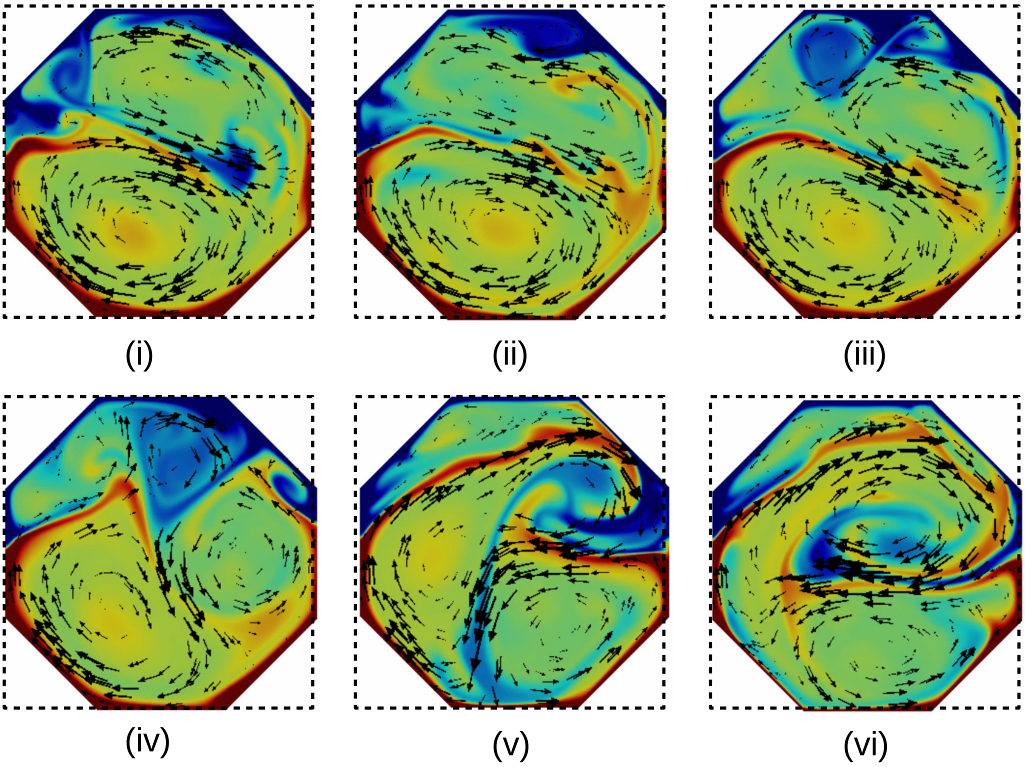

FIG. 32. Steps involved in reversal of two-roll state (i.e., TRSR): Snapshots of the velocity and temperature fields during TRSR at $t/\tau = 10,897$ (i), 10 918 (ii), 10 930 (iii), 10 936 (iv), 10 942 (v), and 10 945 (vi). The dimensionless temperature, $(T - T_c)/\Delta T$, which ranges from 0.3 (blue) to 0.7 (red). Black small arrows for the velocity field. Simulation for $\mathrm{Ra} = 10^8$ and $\mathrm{Pr} = 1.8$.

for $\alpha = 12^\circ$ to 45° reversals take place by both UCR and TRSR for $\mathrm{Ra} > 10^7$. For $\alpha = 12^\circ$ reversal frequencies obtained from UCR and TRSR state are very close to each other. For $\alpha \geqslant 24^\circ$ reversals by TRSR are more frequently happens when compared to UCR. For $\alpha \geqslant 24^\circ$ the dipole mode becomes dominant and leads to an increase in reversal frequency by the TRSR state.

In Fig. 32 we have shown destabilization of two-roll state. An additional secondary roll is generated in the region between the top and the right side conduction walls. The created secondary roll grows with time and merges with one of the rolls having the same direction of rotation. The other roll moves towards the bottom (or top) from the top (or bottom) plate, and that reverses the direction of rotation. See animation 3(b) in the Supplemental Material [45] for more details.

---

[1] S. Kalogirou, Thermal performance, economic and environmental life cycle analysis of thermosiphon solar water heaters, Sol. Energy **83**, 39 (2009).

[2] S. Kumar, Natural convective heat transfer in trapezoidal enclosure of box-type solar cooker, Renewable Energy **29**, 211 (2004).

[3] K. Hadad, A. Rahimian, and M. R. Nematollahi, Numerical study of single and two-phase models of water/Al_2O_3 nanofluid turbulent forced convection flow in VVER-1000 nuclear reactor, Ann. Nucl. Energy **60**, 287 (2013).

[4] H. M. S. Hussein, M. A. Mohamad, and A. S. El-Asfouri, Transient investigation of a thermosyphon flat-plate solar collector, Appl. Therm. Eng. **19**, 789 (1999).

[5] G. Ziskind, V. Dubovsky, and R. Letan, Ventilation by natural convection of a one-story building, Energy Build. **34**, 91 (2002).

[6] M. Schwarzschild, Convection in stars, Astrophys. J. **134**, 1 (1961).

[7] F. Cattaneo, T. Emonet, and N. Weiss, On the interaction between convection and magnetic fields, Astrophys. J. **588**, 1183 (2003).

[8] A. Lenardic, L.-N. Moresi, A. M. Jellinek, and M. Manga, Continental insulation, mantle cooling, and the surface area of oceans and continents, Earth Planet. Sci. Lett. **234**, 317 (2005).

[9] P. Li and J. Liu, Self-driven electronic cooling based on thermosyphon effect of room temperature liquid metal, J. Electron. Packaging **133**, 041009 (2011).

[10] S. Grossmann and D. Lohse, Fluctuations in turbulent Rayleigh–Bénard convection: The role of plumes, Phys. Fluids **16**, 4462 (2004).

[11] G. Ahlers, S. Grossmann, and D. Lohse, Heat transfer and large scale dynamics in turbulent Rayleigh–Bénard convection, Rev. Mod. Phys. **81**, 503 (2009).

[12] D. Lohse and K.-Q. Xia, Small-scale properties of turbulent Rayleigh-Bénard convection, Annu. Rev. Fluid Mech. **42**, 335 (2010).

[13] M. K. Verma, A. Kumar, and A. Pandey, Phenomenology of buoyancy-driven turbulence: Recent results, New J. Phys. **19**, 025012 (2017).

[14] M. K. Verma, *Physics of Buoyant Flows: From Instabilities to Turbulence* (World Scientific, Singapore, 2018).

[15] K. Sugiyama, R. Ni, R. J. A. M. Stevens, T. S. Chan, S.-Q. Zhou, H.-D. Xi, C. Sun, S. Grossmann, K.-Q. Xia, and D. Lohse, Flow Reversals in Thermally Driven Turbulence, Phys. Rev. Lett. **105**, 034503 (2010).

[16] M. Chandra and M. K. Verma, Dynamics and symmetries of flow reversals in turbulent convection, Phys. Rev. E **83**, 067303 (2011).

[17] M. Chandra and M. K. Verma, Flow Reversals in Turbulent Convection Via Vortex Reconnections, Phys. Rev. Lett. **110**, 114503 (2013).

[18] A. Libchaber, From chaos to turbulence in Bénard convection, Proc. R. Soc. A **413**, 63 (1987).

[19] D. A. Egolf, I. V. Melnikov, W. Pesch, and R. E. Ecke, Mechanisms of extensive spatiotemporal chaos in Rayleigh-Bénard convection, Nature (London) **404**, 733 (2000).

[20] E. D. Siggia, High Rayleigh number convection, Annu. Rev. Fluid Mech. **26**, 137 (1994).

[21] S. B. Pope, *Turbulent Flows* (Cambridge University Press, Cambridge, 2000).

[22] D. Lohse and F. Toschi, Ultimate State of Thermal Convection, Phys. Rev. Lett. **90**, 034502 (2003).

[23] E. P. van der Poel, R. J. A. M. Stevens, and D. Lohse, Connecting flow structures and heat flux in turbulent Rayleigh-Bénard convection, Phys. Rev. E **84**, 045303 (2011).

[24] E. P. van der Poel, R. J. A. M. Stevens, K. Sugiyama, and D. Lohse, Flow states in two-dimensional Rayleigh-Bénard convection as a function of aspect-ratio and Rayleigh number, Phys. Fluids **24**, 085104 (2012).

[25] F. Ravelet, A. Chiffaudel, and F. Daviaud, Supercritical transition to turbulence in an inertially driven von Kármán closed flow, J. Fluid Mech. **601**, 339 (2008).

[26] S. G. Huisman, R. C. A. van der Veen, C. Sun, and D. Lohse, Multiple states in highly turbulent Taylor–Couette flow, Nat. Commun. **5**, 3820 (2014).

[27] D. S. Zimmerman, S. A. Triana, and D. P. Lathrop, Bi-stability in turbulent, rotating spherical Couette flow, Phys. Fluids **23**, 065104 (2011).

[28] E. Brown, A. Nikolaenko, and G. Ahlers, Reorientation of the Large-Scale Circulation in Turbulent Rayleigh–Bénard Convection, Phys. Rev. Lett. **95**, 084503 (2005).

[29] E. Brown and G. Ahlers, Rotations and cessations of the large-scale circulation in turbulent Rayleigh–Bénard convection, J. Fluid Mech. **568**, 351 (2006).

[30] G. A. Glatzmaiers and P. H. Roberts, A three-dimensional self-consistent computer simulation of a geomagnetic field reversal, Nature (London) **377**, 203 (1995).

[31] G. A. Glatzmaier, R. S. Coe, L. Hongre, and P. H. Roberts, The role of the Earth's mantle in controlling the frequency of geomagnetic reversals, Nature (London) **401**, 885 (1999).

[32] J. P. Valet, A. Fournier, V. Courtillot, and E. Herrero-Bervera, Dynamical similarity of geomagnetic field reversals, Nature (London) **490**, 89 (2012).

[33] E. van Doorn, B. Dhruva, K. R. Sreenivasan, and V. Cassella, Statistics of wind direction and its increments, Phys. Fluids **12**, 1529 (2000).

[34] K. R. Sreenivasan, A. Bershadskii, and J. J. Niemela, Mean wind and its reversal in thermal convection, Phys. Rev. E **65**, 056306 (2002).

[35] F. F. Araujo, S. Grossmann, and D. Lohse, Wind Reversals in Turbulent Rayleigh-Bénard Convection, Phys. Rev. Lett. **95**, 084502 (2005).

[36] H.-D. Xi and K.-Q. Xia, Azimuthal motion, reorientation, cessation, and reversal of the large-scale circulation in turbulent thermal convection: A comparative study in aspect ratio one and one-half geometries, Phys. Rev. E **78**, 036326 (2008).

[37] A. Castillo-Castellanos, A. Sergent, and M. Rossi, Reversal cycle in square Rayleigh-Bénard cells in turbulent regime, J. Fluid Mech. **808**, 614 (2016).

[38] Y. Wang, P.-Y. Lai, H. Song, and P. Tong, Mechanism of large-scale flow reversals in turbulent thermal convection, Sci. Adv. **4**, eaat7480 (2018).

[39] X. Chen, S.-D. Huang, K.-Q. Xia, and H.-D. Xi, Emergence of substructures inside the large-scale circulation induces transition in flow reversals in turbulent thermal convection, J. Fluid Mech. **877**, R1 (2019).

[40] X. Chen, D.-P. Wang, and H.-D. Xi, Reduced flow reversals in turbulent convection in the absence of corner vortices, J. Fluid Mech. **891**, R5 (2020).

[41] H. Jasak, A. Jemcov, and Z. Tukovic, OpenFOAM: A C++ library for complex physics simulations, in *International Workshop on Coupled Methods in Numerical Dynamics*, Vol. 1000 (IUC Dubrovnik Croatia, 2007), pp. 1–20.

[42] A. Pandey, A. Kumar, A. G. Chatterjee, and M. K. Verma, Dynamics of large-scale quantities in Rayleigh-Bénard convection, Phys. Rev. E **94**, 053106 (2016).

[43] A. Pandey and M. K. Verma, Scaling of large-scale quantities in Rayleigh-Bénard convection, Phys. Fluids **28**, 095105 (2016).

[44] Y. Nandukumar, S. Chakraborty, M. K. Verma, and R. Lakkaraju, On heat transport and energy partition in thermal convection with mixed boundary conditions, Phys. Fluids **31**, 066601 (2019).

[45] See Supplemental Material at http://link.aps.org/supplemental/10.1103/PhysRevFluids.5.103501 for animations of the flow.

[46] R. Ni, S.-D. Huang, and K.-Q. Xia, Reversals of the large-scale circulation in quasi-2D Rayleigh–Bénard convection, J. Fluid Mech. **778**, R5 (2015).

[47] Q. Wang, S.-N. Xia, B.-F. Wang, D.-J. Sun, Q. Zhou, and Z.-H. Wan, Flow reversals in two-dimensional thermal convection in tilted cells, J. Fluid Mech. **849**, 355 (2018).

[48] L. N. Howard, Convection at high Rayleigh number, in *Proceedings of the 11th International Congress of Applied Mathematics on Applied Mechanics, Munich, 1964* (Springer, New York, 1966), p. 1109.

[49] E. Villermaux, Memory-Induced Low Frequency Oscillations in Closed Convection Boxes, Phys. Rev. Lett. **75**, 4618 (1995).

[50] E. Brown and G. Ahlers, Large-Scale Circulation Model for Turbulent Rayleigh–Bénard Convection, Phys. Rev. Lett. **98**, 134501 (2007).

[51] J. P. Gollub and S. V. Benson, Many routes to turbulent convection, J. Fluid Mech. **100**, 449 (1980).

[52] B. Kaulakys, J. Ruseckas, V. Gontis, and M. Alaburda, Nonlinear stochastic models of noise and $1/f$ power-law distributions, Physica A **365**, 217 (2006).

[53] M. K. Verma, S. C. Ambhire, and A. Pandey, Flow reversals in turbulent convection with free-slip walls, Phys. Fluids **27**, 047102 (2015).

[54] Q. Wang, Z.-H. Wan, R. Yan, and D.-J. Sun, Flow organization and heat transfer in two-dimensional tilted convection with aspect ratio 0.5, Phys. Fluids **31**, 025102 (2019).

[55] P. K. Mishra, A. K. De, M. K. Verma, and V. Eswaran, Dynamics of reorientations and reversals of large-scale flow in Rayleigh–Bénard convection, J. Fluid Mech. **668**, 480 (2011).

[56] P. J. Sakievich, Y. T. Peet, and R. J. Adrian, Large-scale thermal motions of turbulent Rayleigh-Bénard convection in a wide aspect-ratio cylindrical domain, Int. J. Heat Fluid Flow **61**, 183 (2016).

[57] Y. Zhang, Y.-X. Huang, N. Jiang, Y.-L. Liu, Z.-M. Lu, X. Qiu, and Q. Zhou, Statistics of velocity and temperature fluctuations in two-dimensional Rayleigh-Bénard convection, Phys. Rev. E **96**, 023105 (2017).

[58] S. Kenjereš, Heat transfer enhancement induced by wall inclination in turbulent thermal convection, Phys. Rev. E **92**, 053006 (2015).

[59] S. Wagner and O. Shishkina, Heat flux enhancement by regular surface roughness in turbulent thermal convection, J. Fluid Mech. **763**, 109 (2015).

[60] R. Lakkaraju, R. J. A. M. Stevens, R. Verzicco, S. Grossmann, A. Prosperetti, C. Sun, and D. Lohse, Spatial distribution of heat flux and fluctuations in turbulent Rayleigh-Bénard convection, Phys. Rev. E **86**, 056315 (2012).

[61] E. P. van der Poel, R. J. A. M. Stevens, and D. Lohse, Comparison between two-and three-dimensional Rayleigh–Bénard convection, J. Fluid Mech. **736**, 177 (2013).

[62] E. S. C. Ching and W. S. Tam, Aspect-ratio dependence of heat transport by turbulent Rayleigh-Bénard convection, J. Turbul. **7**, N72 (2006).

[63] J. Bailon-Cuba, M. S. Emran, and J. Schumacher, Aspect ratio dependence of heat transfer and large-scale flow in turbulent convection, J. Fluid Mech. **655**, 152 (2010).

[64] L. P. Kadanoff, Turbulent heat flow: Structures and scaling, Phys. Today **54**, 34 (2001).

[65] B. Castaing, G. Gunaratne, F. Heslot, L. Kadanoff, A. Libchaber, S. Thomae, X.-Z. Wu, S. Zaleski, and G. Zanetti, Scaling of hard thermal turbulence in Rayleigh-Bénard convection, J. Fluid Mech. **204**, 1 (1989).

[66] John C. Wyngaard, *Turbulence in the Atmosphere* (Cambridge University Press, Cambridge, 2010).

[67] A. P. Vincent and D. A. Yuen, Plumes and waves in two-dimensional turbulent thermal convection, Phys. Rev. E **60**, 2957 (1999).

[68] S. Grossmann and D. Lohse, Scaling in thermal convection: A unifying theory, J. Fluid Mech. **407**, 27 (2000).

[69] R. M. Kerr and J. R. Herring, Prandtl number dependence of Nusselt number in direct numerical simulations, J. Fluid Mech. **419**, 325 (2000).

[70] K.-Q. Xia, S. Lam, and S.-Q. Zhou, Heat-Flux Measurement in High-Prandtl-Number Turbulent Rayleigh-Bénard Convection, Phys. Rev. Lett. **88**, 064501 (2002).

[71] M. Breuer, S. Wessling, J. Schmalzl, and U. Hansen, Effect of inertia in Rayleigh-Bénard convection, Phys. Rev. E **69**, 026302 (2004).

[72] Q. Zhou and K.-Q. Xia, Thermal boundary layer structure in turbulent Rayleigh-Bénard convection in a rectangular cell, J. Fluid Mech. **721**, 199 (2013).

[73] J. D. Scheel, E. Kim, and K. R. White, Thermal and viscous boundary layers in turbulent Rayleigh-Bénard convection, J. Fluid Mech. **711**, 281 (2012).

[74] N. Shi, M. S. Emran, and J. Schumacher, Boundary layer structure in turbulent Rayleigh-Bénard convection, J. Fluid Mech. **706**, 5 (2012).

[75] S. Wagner, O. Shishkina, and C. Wagner, Boundary layers and wind in cylindrical Rayleigh-Bénard cells, J. Fluid Mech. **697**, 336 (2012).

[76] K. Petschel, S. Stellmach, M. Wilczek, J. Lülff, and U. Hansen, Kinetic energy transport in Rayleigh-Bénard convection, J. Fluid Mech. **773**, 395 (2015).

[77] A. Parodi, J. von Hardenberg, G. Passoni, A. Provenzale, and E. A. Spiegel, Clustering of Plumes in Turbulent Convection, Phys. Rev. Lett. **92**, 194503 (2004).